

Master Thesis

Microscopy study of the onset of plastic deformation and modeling creep behavior of AISI 420 stainless steel

Gerrit Zijlstra
1694499

Under the supervision of:
M. Groen (Philips Drachten)
Dr. ir. V. Ocelík (Rijksuniversiteit Groningen)
Prof. Dr. J. Th. M. De Hosson (Rijksuniversiteit Groningen)

2013-2014



**university of
 groningen**



This page is intentionally left blank.

Abstract

The aim of this study is to experimentally optimize a creep model for AISI 420 stainless steel and use this model to predict the shape change of shaver caps during a heat treatment. This is obtained by investigating the microstructure, mechanical properties and thermal expansion characteristics, in the range 22 °C - 800 °C. The material in the as-received condition is fully ferritic, textured due to rolling and contains a small amount of stored strain. The anisotropic behavior is observed in Young's modulus and very small in the volume drop at the start of austenization at 809 °C. With a cooling rate higher than 50 °C/min, perlite is avoided and only martensite forms at about 360 °C. For creep at 500 °C dislocation climb, and at 600 °C dislocation glide is rate controlling. Creep enables the material to relax residual stresses. The implementation of the creep model in the Philips FEM-solver Crystal, is validated with creep and stress relaxation tests. Application of the calibrated creep model on the calculations of a cup with heat treatment shows distortions of the same order of magnitude shaver caps have.

This page is intentionally left blank.

Contents

1	Introduction	3
1.1	Philips Consumer lifestyle	3
1.2	The quest	5
2	Test setup and experimental procedure	7
2.1	Material	7
2.2	Electron microscopy	7
2.3	Dilatometry	9
2.4	Tensile tests	10
2.4.1	Setup	10
2.4.2	Equipment and modifications for optimization	10
2.4.3	Determination of flow stress and Elastic modulus	15
2.5	Stress relaxation test	17
3	Results and Discussion	19
3.1	Microstructural analysis	19
3.2	Transformation characteristics	30
3.3	Mechanical properties	34
4	Experimental calibration of constitutive equation for creep	46
4.1	Calibration with creep-data from literature	47
4.2	Calibration with experimental creep-data	50
5	Finite Element Method implementation	52
6	Conclusions and outlook	62
7	Acknowledgments	64
	References	65

Appendices	68
Appendix A	68
Appendix B	73
Appendix C	75

1 Introduction

Today's consumer products need more and more high precision metallic parts to match the increasing quality demands of consumers. These parts are often manufactured in 20 or more processing steps, including: shaping operations, heat treatment, finishing operations and assembly. Defects and irregularities that occur in the parts during the production process need to be decreased and controlled. Therefore, in-depth knowledge of the micro structure and surface modification is required. This knowledge can be used to calibrate and validate constitutive models that are the backbone of simulation processes. Simulations of material behavior are key for optimization of current manufacturing and studying the possible benefits of new production methods.

For this purpose the University of Groningen and Philips Drachten collaborate in a joint research project called BESTSHAVING (BEtter STEel for SHAVING). Goal is to perform a microscopy study of plastic deformation, anisotropy, recovery and air passivation in stainless steels for shaver caps. The work done for this thesis is part of the BESTSHAVING project with focus on the creep behavior during heating of shaving steel.

1.1 Philips Consumer lifestyle

Philips Drachten is part of the division Consumer Lifestyle (CL). At this site, a variety of household appliances like coffeemakers, vacuum cleaners and hairdryers are developed and improved in an advanced research center. Philips Drachten may be known best for producing and developing electrical shavers, for which it holds a leading position worldwide.

Philips produces rotary electrical shavers. Nowadays, shavers consist of one shaving head with three elements (figure 1). Each element consist of a shaver cap, which is placed on the skin, and a cutter which rotates inside the cap (figure 2).



Figure 1: *Shaver head with three elements.*

The production of shaver caps is split up in 3 steps: forming, hardening and finishing. The forming process starts with a steel strip which is fed to a (stamping) press. The cap will receive it's shape in several stages of cold forming, including deepdrawing. Then, the caps will be cut out of the strips and go into the belt furnace of figure 3. The temperature inside the furnace is high enough to enable the caps to transform from the ferritic phase into the austenitic phase. By rapid cooling afterwards, the austenite transforms to a (much harder) martensite. This process is therefore known as hardening. To relief internal stresses, the caps undergo a second heat treatment in which they are annealed at 250 °C. Distortions and irregularities on the cap that remain after the forming and hardening steps, have to be removed to obtain a high quality product that matches the needs of the consumer. This finishing process is done by electrochemical processing (ECP), which is an expensive step due to the amount of required (electrical) energy, numerous machines, and the slow speed of the process.

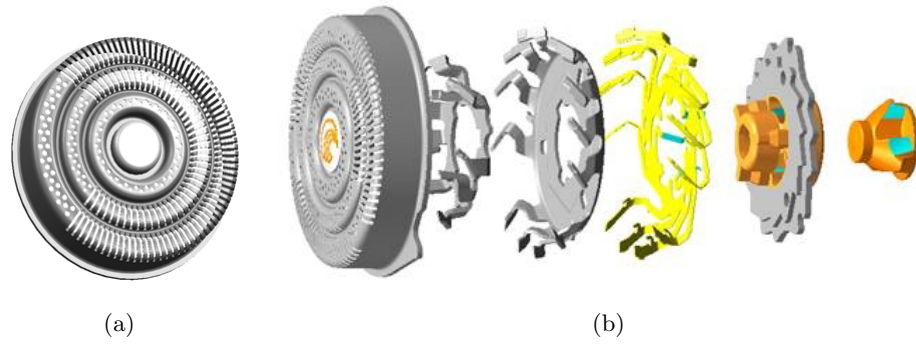
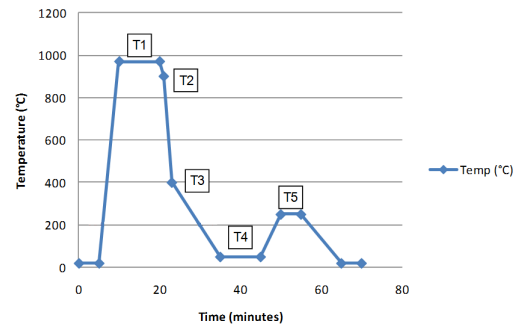


Figure 2: *Shaver cap (a) and cutter (b).*



(a)

(b)

Figure 3: *The belt furnace (a) and its temperature-time profile (b).*

1.2 The quest

The surface of the shaver caps needs to be smooth on the outside, because distortions or burs can irritate the skin during shaving. A polished surface on the inside of the cap is also very important, since the cutter rotates inside the cap very close to the surface (as seen in figure 2). A rough surface can damage the cutter and reduce its performance. It is therefore necessary to produce a distortion-free shaver cap, either by the prevention of distortions during manufacturing, or by removing them afterwards with electro-chemical polishing. Since the latter is an expensive process, it is valuable to focus on the former.

It is observed that distortions from the forming stage are doubled during the hardening process, which is graphically shown in figure 4. The treatment of heating to a 1000 °C is thus a very critical stage. If the influential processes can be quantified and used in a model, it is possible to predict the influence of certain aspects in the forming stage on the shape of the cap after hardening. New tools for the press for forming could then be tested in advance by simulating the products the tool would make and the distortions it will cause. The design of the press could then be adjusted on forehand, to optimize its capability to produce caps with less distortions.

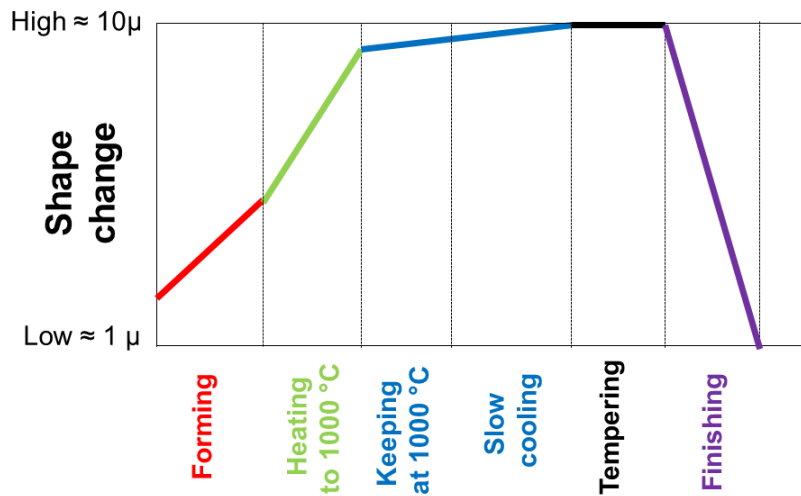


Figure 4: *Shape changes on the cap due to production steps.*

The aim of this study is to optimize an existing model that can predict the shape change of the caps during the heat treatment. Different processes and properties of the material are active during hardening. We surmise that anisotropy, residual stresses after forming, phase changes, microstructure and mechanical properties interact with each other in a way that:

i) with the increase of temperature, mechanical properties as the yield point and the elastic (Young's) modulus decrease. Therefore residual stresses due to deep drawing, can induce plastic deformation as the stresses become higher than the (decreasing) yield point. Stresses below the yield point can also cause plastic deformation due to thermally activated creep processes. The effect of temperature on the flow stress and elastic modulus will be investigated by performing tensile tests. For the influence of temperature and load on the creep rate, creep tests will be done.

ii) the microstructure changes and therefore the mechanical properties. With EBSD, the grain structure

will be mapped to check growth or nucleation. This technique also will be used to reveal if there is texture (indicating anisotropy), and if this changes after a heat treatment.

iii) possible anisotropy may influence the yield point, elastic modulus and thermal expansion. Tensile tests in different directions will be done to quantify the possible difference. Dilatometer tests can indicate the effect of anisotropy on the thermal expansion. They can also be used to investigate the existence of irreversible shape changes in the ferritic phase.

The knowledge of these parameters will be used to perform an experimental validation of a creep model. The model will be used in a finite element solver to predict shape change as the result of residual stresses during a heat treatment.

2 Test setup and experimental procedure

The experimental techniques, material and procedures for the above tests will be outlined in this section.

2.1 Material

The material studied is a martensitic stainless chromium steel with a low carbon content. The chemical composition is displayed in table 1. Since the specifications are in the range of table 2, we can classify it as an AISI 420 type of stainless steel. Within Philips, this material is known as N004.

C	Cr	Si	Mn	P	S	Mo	Fe
0.32	13.7	0.15	0.30	≤ 0.025	≤ 0.010	-	Bal.

Table 1: Chemical composition of N004 in weight percent [1].

C	Cr	Si	Mn	P	S	Fe
min 0.15	12 - 14	1	1	0.04	0.030	Bal.

Table 2: Specifications of AISI 420. Given values are upper limits in weight percent, unless indicated otherwise [2].

As received from the manufacturer, the steel is in the ferritic phase and wrapped in coils. Samples were cut out two different coils. One set was cut from a coil of 38 mm width and 0.3 mm thick material. The second set from a wide band coil of 45 cm, with a thickness of 0.5 mm.

2.2 Electron microscopy

The microstructure of the material has been investigated with the use of Electron Backscatter Diffraction (EBSD). This technique requires a Scanning Electron Microscope (here a Philips XL30 SEM FEG) with an EBSD detector (TSL EBSD/OIM with digital camera). An electron gun creates a focused beam of electrons which interact with the atoms in the sample. Part of these electrons are back-scattered with energies close to the energy of the interacted beam and a small fraction of these electrons are diffracted on crystal planes present in the sample. In order to detect these diffracted electrons, the sample is tilted to an angle of about 70 degrees from the horizontal plane. For a particular crystal, the backscattered electrons are diffracted at particular angles, depending on the periodic lattice spacings by Bragg's law. The resulting diffraction pattern is detected by a CCD camera. The combined pattern of multiple different refraction planes is known as a Kikuchi pattern (figure 5(a)). The bright peaks of this image are selected and displayed in Hough space as points. These points are indexed using a Hough transformation. Hereby a line through a point is drawn, to which the distance of a perpendicular line to the origin is the smallest [3]. The drawn lines can be indexed by Miller indices 5(b), since angles between the drawn lines represent angles between the lattice planes. Hereby, the Kikuchi pattern of every scanned crystal is translated to a phase and orientation of that crystal in every inspected point at the sample surface.

The three axes of the orientation of the crystal can be mapped on a 2D-plane with a stereographic projection (an interactive animation can be found at [4]). In figure 6(a) an axis is represented by the line OP, with the projection p of the point P on the 2D plane spanned by RD and TD. Projections on this plane are called pole figures. When the grains in a material have a random crystallographic orientation, the pole figure will look as figure 6(b). When there is a degree of texture, grains tend to orient in the same direction and the poles will accumulate at specific directions [4] (see figure 6(c)).

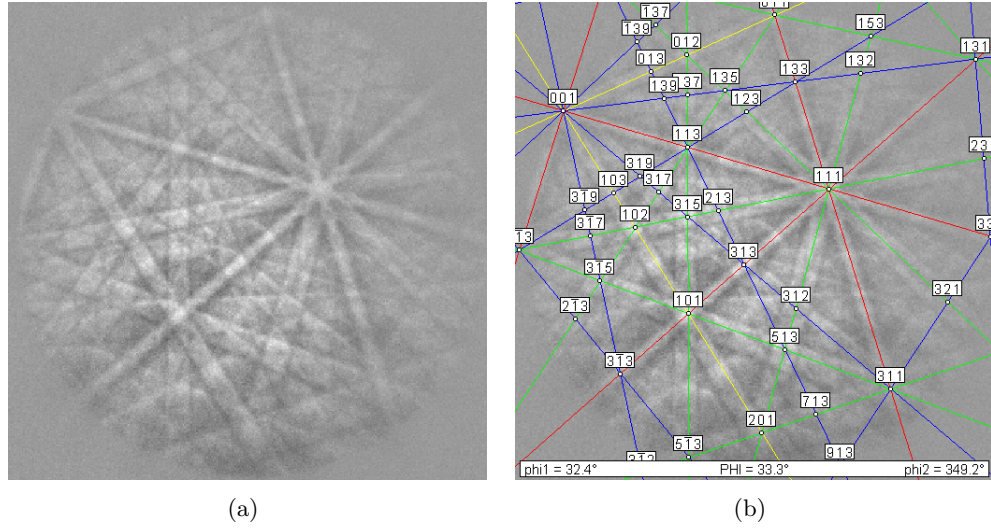


Figure 5: (a) Typical Kikuchi pattern, indexed as ferrite (b).

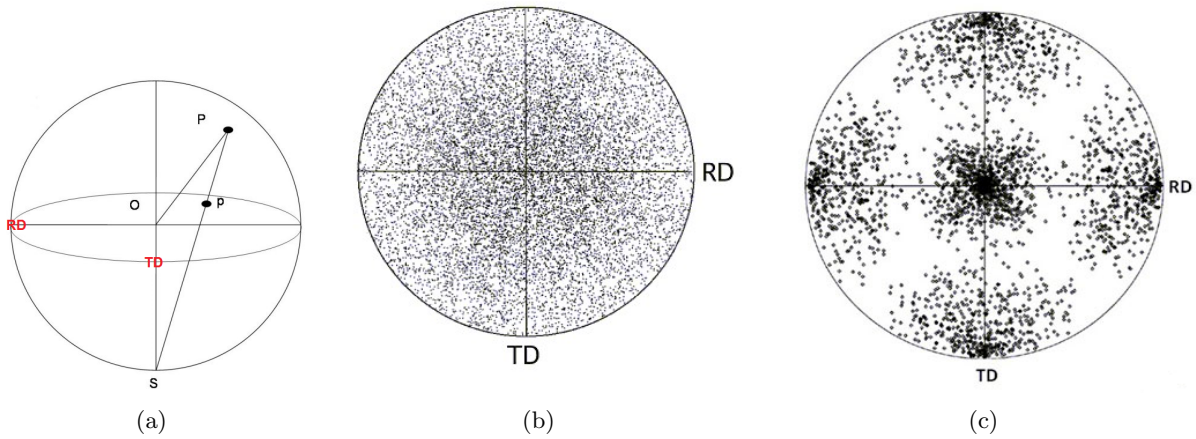


Figure 6: (a) stereographic projection of an axis on a plane [23]. Pole figures of: (b) material with random crystal orientations, and (c) material with a degree of texture [4].

For chemical composition analysis, energy dispersive X-ray spectroscopy (EDS) has been done with the use of a Philips XL30 ESEM FEG with an EDAX EDS detector.

2.3 Dilatometry

Dilatometer tests have been performed on a TMA Q400 EM dilatometer of TA Instruments [10]. The dilatometer can measure the expansion of the sample by applying a quartz pillar on top of the sample. This very sensitive pillar only applies a load of 1 N ($\sim 0.2\text{MPa}$) on the sample. The sample can be heated and cooled with constant rates, as well heated with a modulating rate. By applying a sine wave heating profile, the rate change of the sample length with respect to time can be divided into two components [11]:

$$\frac{dL}{dt} = \alpha \frac{dT}{dt} + f(t, T), \quad (1)$$

with α the linear thermal expansion coefficient. With the help of this equation, software is able to separate the change in length in a reversible and irreversible part.

Samples with a length of about 12 mm, width of 10 mm and 0.5 mm thickness were made. To prevent buckling and constraining by e.g. a quartz holder, the sample was prepared to stand alone. This has been done by making two cuts: one from the top to the center and one from the bottom to the center. The two sides were folded inside, creating an L-shape sample (see figure 7), which can stand by itself. The induced strains by the bending are very local and concentrate around the bending point, therefore they have little influence on the measurement.

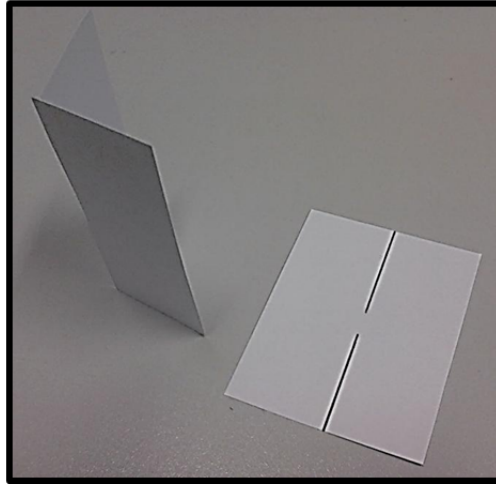


Figure 7: *Preparation of 0.5 mm thick sample for dilatometer.*

2.4 Tensile tests

Tensile tests were performed with a setup consisting of a Zwick / Roell Z30 tensile bench, equipped with a three-zone Maytec furnace with induction heating elements and a Fiedler Laser Extensometer as shown in figure 8.

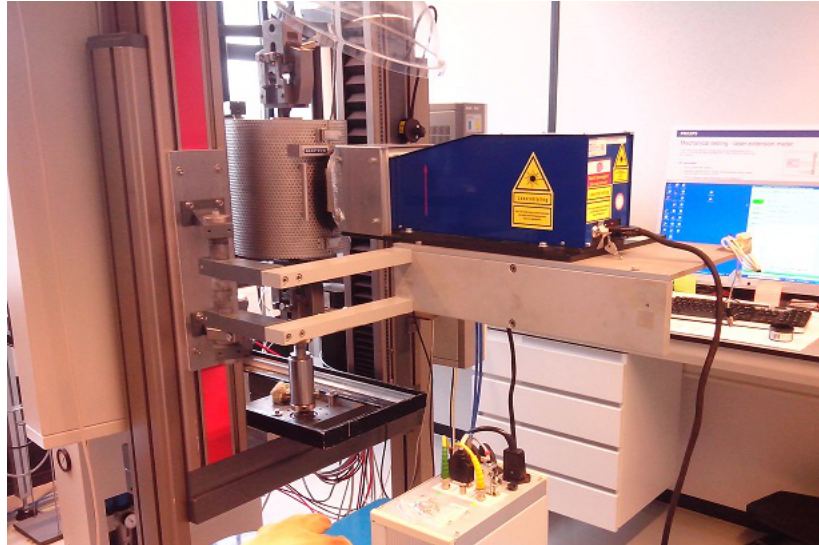


Figure 8: *Tensile bench with the laser extensometer placed in front of the furnace.*

2.4.1 Setup

The elevated temperature tensile tests were performed in the following procedure. First, the furnace is pre-heated to the desired temperature. Once this temperature is reached, the tensile bar was placed in the furnace and clamped in the top grip of the bench. Therefore the tensile bar could expand during its heating trajectory. Then the furnace is closed and the top and bottom holes are filled with mineral wool (see figure 14). After a ceramic tube with glass for the laser is inserted (closing the porthole of the laser to prevent air flow), the furnace has to be heated again. Once the target temperature of the furnace is reached, five minutes are taken for the system to stabilize. After that, only a fluctuation in the furnace temperature of $\pm 1^\circ\text{C}$ was observed. Since the material has a thickness of 0.5 mm, it is assumed that the temperature of the tensile bar is the same as the furnace after stabilization. At this moment the bottom grip is closed and the Laser Extensometer (LEX) on its table is placed in front of the ceramic tube. The position of the LEX has to be adjusted before every measurement to obtain the maximum signal.

2.4.2 Equipment and modifications for optimization

The used Laser Extensometer (LEX) is a P-100 from Fiedler Optoelektronik, with specifications shown in table 3.

The LEX has a rotating deflector in the Scanner which projects a laser beam parallel on a tensile bar.

Scan Range on Specimen	100 mm
Working Distance	100 - 300 mm
Resolution (micron)	0.25 μm
Accuracy (DIN EN 10002-4)	Class 0.5; 1
Scanning rate	50 Hz
Duration of each Scan at Specimen	5.0 ms
Scan Speed on Specimen	20 m/s
Specimen Surface	flat or rough

Table 3: Specifications of Fiedeler P-100 laser extensometer, from [5].

The reflected beam from the specimen is redirected by a mirror into the Receiver, as shown in figure 9. Laser light reflected by markers on the tensile bar is measured with a photo diode in the receiver. The electrical signal from the photo diode comes in as a function of time. Since the scanning speed of the LEX is known, this signal can be transformed to a signal as a function of position. As shown in figure 10, the second derivative of the signal as a function of time is taken. The point where the second derivative goes through the x-axis, represents the transition between stripe and sample.

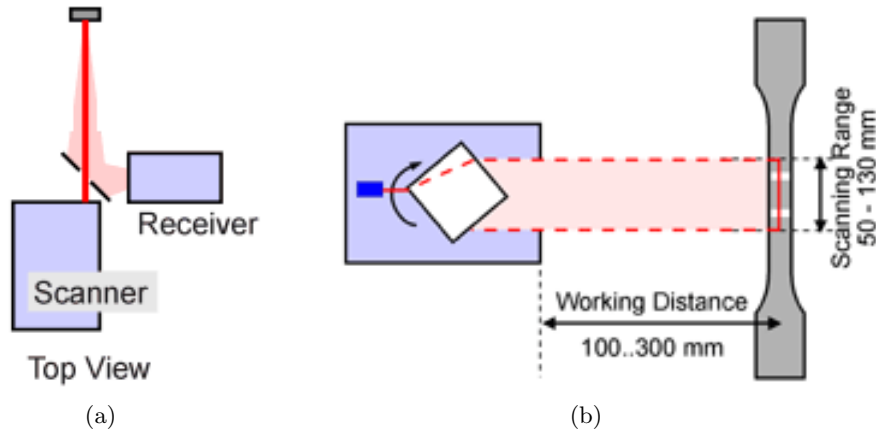


Figure 9: (a) Top view of LEX [6] and (b) projection of laser beam on a tensile bar [5]

The tensile bars are laser cut from a 0.5 mm thick plate with a length of 43 mm and width of 20 mm. Since the LEX determines the position of the marker at the transition of the marker and the background, the contrast between the tensile bar and the marker should be very large, and noise should be avoided as much as possible. Therefore, the shiny metal surface is treated with a heat resistant black paint along the bar. Then, two markers are applied with heat resistant white paint. These paints work well to temperatures as high as 700 °C. Above this temperature, the black paint only gets a bit fainter, but the white paint becomes dark. We have experimented with white markers consisting of titanium dioxide. This has been done by dissolving the white titanium dioxide powder at ethanol, and applying it to the tensile bar with a syringe (see figure 11). After the ethanol is evaporated, a delicate layer of TiO_2 remains on the tensile bar. This layer is very brittle and therefore not very practical to use. When the tensile bar is elongated, the layer starts to break and discerps from the bar. This problem can be reduced by applying TiO_2 on the wet white paint. The result is an enhanced contrast (even after 6 hours at 800 °C) and the flexibility of the paint prevents the TiO_2 layer to break off.

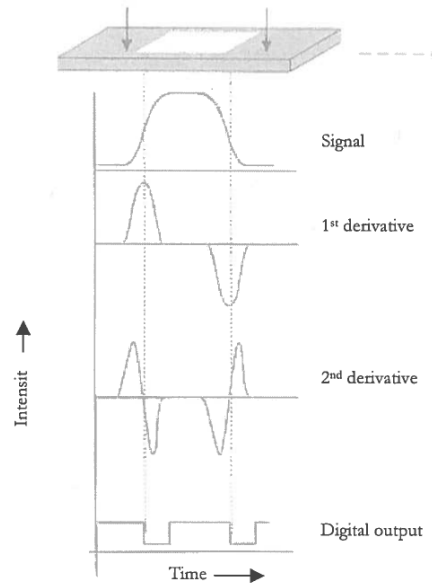


Figure 10: *Determination of the transition between stripe and sample [7].*



Figure 11: *Applying dissolved titanium dioxide on a tensile bar with a syringe.*

The black underground does not only increase the contrast of the marker, it also suppresses the reflection of the laser (figure 12).

As shown in figure 10, the position of the marker is determined by taking the second derivative of the signal. Noise causes fluctuations in the signal and covers a part of the signal, therefore influencing the derivatives and thus the determination of the marker position. Reflection of the laser beam from the tensile bar and parts of the furnace have been suppressed by applying a non-shining black heat resistant paint (see also figure 15). Switching off the lights in the laboratory and shielding off natural light also helped to reduce the background noise. The LEX (with wavelength of 670 nm) has an Infra Red filter

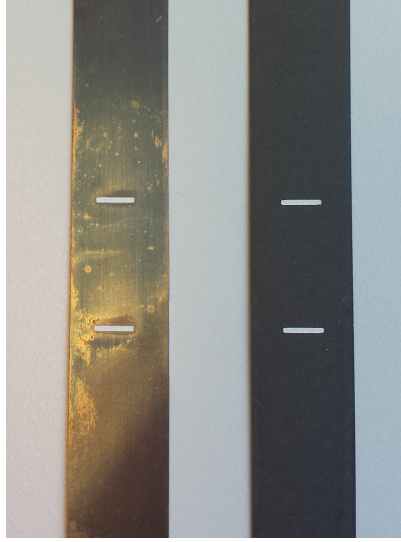


Figure 12: *Painted (right) and non-painted (left) tensile bars after a heat treatment of 10 minutes at 600°C. The oxidation layer on the left bar is still highly reflective.*

in the receiver which blocks light above a wavelength of 780 nm. From Wien's displacement law:

$$\lambda_{max}T = 2.9 * 10^6 \text{ nmK}, \quad (2)$$

we have $\lambda_{max} = 2470 \text{ nm}$ for 900°C. The peak intensity is way above the threshold of the filter, thus radiation of the tensile bar and inductive elements should not be a problem at this temperature.

First tests at high temperature showed a lot of noise. As shown in figure 13, fluctuations of about $1 * 10^{-3}$ occur, which correspond to 25 micrometers.

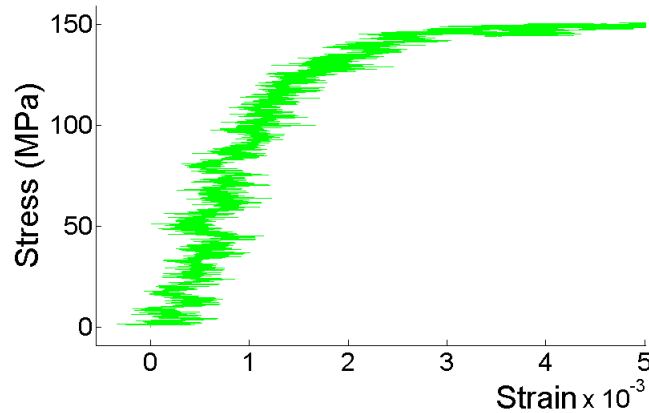


Figure 13: *Noisy measurement of tensile test at 600°C with $\dot{\epsilon} = 0.0001 \text{ s}^{-1}$.*

Due to the huge difference in temperature and the room temperature, a lot of convection exists. Hot air is exhausted at the gap of the furnace where the tensile bar comes out to be clamped, and through the hole in for the laser beam. At the same time air at room temperature is sucked in through the gap at the bottom of the furnace and the lower part of the porthole. The strong convection induces a lot

of turbulence in and outside the furnace. Hot air is less dense than air at room temperature and has therefore a smaller refractive index. Due to the air turbulence, the laser beam goes through a medium with a frequently changing refraction index. Therefore, the amount of reflected light that reaches the receiver is decreasing with increasing turbulence, (i.e. increasing temperature). The remaining light that reaches the receiver can have traveled different paths for the two markers and therefore will be noticed by the receiver with a delay, so the markers appear to be at different places. To prevent and reduce the turbulence, the furnace has been closed as much as possible. First by filling up the gap between the tensile bar and the furnace before every tensile test with mineral wool (see figure 14).

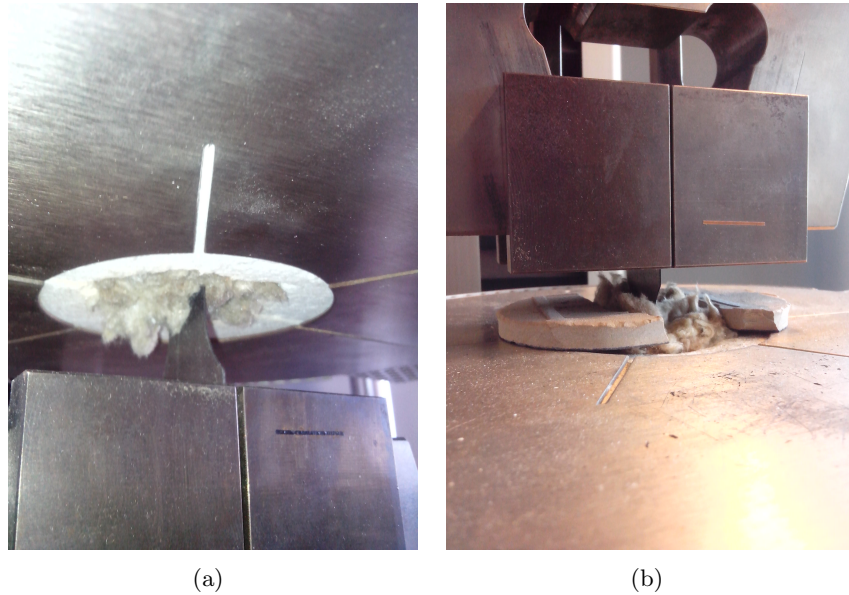


Figure 14: *Bottom and top gap of furnace filled with mineral wool to prevent turbulence.*

Second step was to close the porthole for the laser beam. For this purpose a ceramic tube of Al_2O_3 has been designed. This ceramic does not expand much due to the heat. Therefore the dimensions of the tube could be so precise that it nicely fitted into the porthole in the furnace (figure 15). A piece of heat resistant glass was cut out and placed in the ceramic tube on the outside of the furnace to close the tube, preventing an air flow. The tube was slid into the furnace up to the tensile bar. Therefore the air inside the tube was shielded from any remaining turbulence inside the furnace. After 5 minutes the system is stable and the air in the tube has the same temperature as the furnace and the test can be started.

An improved test is shown in figure 16. The fluctuations at the start of the test are due to adjustments of the tensile bench to achieve the right load. Thereafter the test does not show fluctuations in the length measurement as a result of noise. Due to the improvements in the test setup, noise in the measurements has been reduced to values below $1 \mu m$ which together with typical distance between two marker (~ 50 mm), results in a precision better than: 0.002%.



Figure 15: Ceramic tube closing the porthole of the furnace (glass not visible).

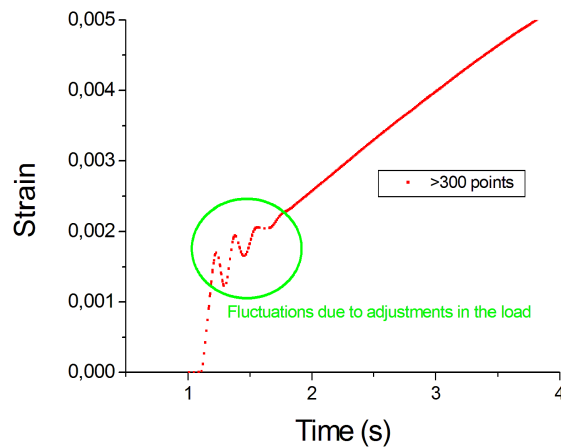


Figure 16: Creep test at 600°C with a tensile load of 100 MPa.

2.4.3 Determination of flow stress and Elastic modulus

Elastic behavior can be observed when a (material) body is loaded. First it will deform, but regain its initial dimensions if the load is removed. At some point, the elastic limit, the load is too big and the body is deformed permanent. When a body is permanently deformed, it has undergone plastic deformation. The relationship of load and deformation in the elastic regime is known as Hooke's law, which implies that strain is proportional to stress. If we put an external load P on a cylindrical bar,

the bar reacts with an internal resisting force $\int \sigma dA$. The equilibrium equation therefore becomes:

$$P = \int \sigma dA, \quad (3)$$

where σ is the stress normal to the cutting plane and A is the area of the cross-section of the bar. If the stress is distributed uniformly over the area A , we get the average stress:

$$\sigma = \frac{P}{A} \quad (4)$$

The average linear (or engineering) strain e is resembled by the ratio of the change in length L and the original length L_0 .

$$e = \frac{\Delta L}{L_0} = \frac{L - L_0}{L_0}, \quad (5)$$

Hooke's law is valid below the elastic limit, therefore the average stress is proportional to the average strain by:

$$\frac{\sigma}{e} = E = \text{constant}, \quad (6)$$

where E is the modulus of elasticity, also called Young's modulus.

Equations (5) and (6) are based on the original dimensions of the bar. However, the dimensions are not constant above the elastic limit. They change constantly during the test, i.e. the bar becomes more narrow during the test. Therefore, the true stress is introduced and defined as:

$$\sigma = \frac{P}{A}, \quad (7)$$

where A is the actual cross section. If we obtain the actual cross section by assuming volume conservation:

$$A = \frac{A_0 L_0}{\Delta L + L_0}, \quad (8)$$

the true stress is given by

$$\sigma = \frac{P}{A_0} \frac{\Delta L + L_0}{L_0} \quad (9)$$

The true strain ϵ is often used to compare strains of samples which have deformed more than 5%, and is defined as:

$$\epsilon = \int_{L_0}^L \frac{dL}{L} = \ln \frac{L}{L_0} \quad (10)$$

Here, the strain is defined as the instantaneous gage length instead of the original gage length. It can be shown that

$$\epsilon = \ln \frac{L}{L_0} = \ln(e + 1) \quad (11)$$

For small strains $\ln(e + 1) \approx e$, therefore the conventional and true strain give the same values.

A true stress-strain curve is frequently called a flow curve because it gives the stress required to cause the metal to flow plastically to any given strain. More details for further reading can be found in [8].

Information from the tensile test is processed in the following way: raw data of the tensile machine, consisting of the distance between the markers (as measured by the LEX) and the force acting on the

tensile bar (as measured by the load cell of the tensile bench), was taken and fed to an own developed MATLAB [9] routine. The true strain has been calculated according to equation (10), where the first (absolute) measurement of the LEX is taken as L_0 . For the true stress, equation (9) is used with A_0 the area given by the initial width and thickness of the tensile bar.

For determination of the E-modulus and flow stress, a pole filter is applied on the vector of the strain. The filter performs a zero-phase digital filtering by processing the data in forward and reverse directions. The filter takes a ratio of a number of sequential points (between 15-50, with equal weight) along the curve.

With these data of the filter, the coefficients p_1 and p_2 of a first order polynomial are calculated in a least squares sense. The resulting function

$$p(x) = p_1 + p_2x \quad (12)$$

is applied on the elastic part of the tensile curve (figure 17(b)). The data between 0.05 and 0.1% strain (indicated by the dotted lines in figure 17(c)) is taken as the elastic part for fitting the E-modulus line. At the same time the function $g(x)$ for the yield point, defined as:

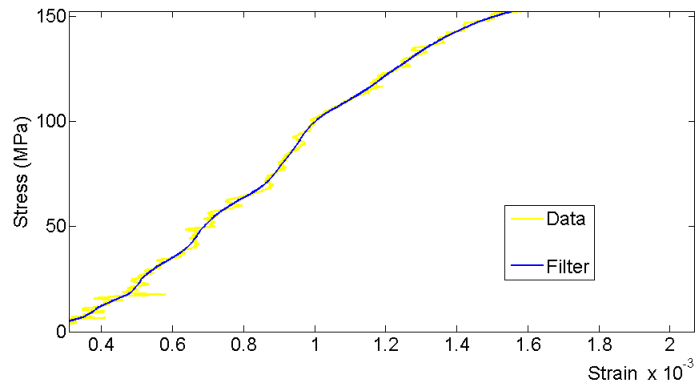
$$g(x) = 0.002 + p_1 + p_2x, \quad (13)$$

is plotted at 0.2% offset from the line $p(x)$ (as shown in figure 17(c)). The intersection of the 0.2% offset and the filter is the yield point (by convention) and the corresponding stress (of the yield point) the flow stress.

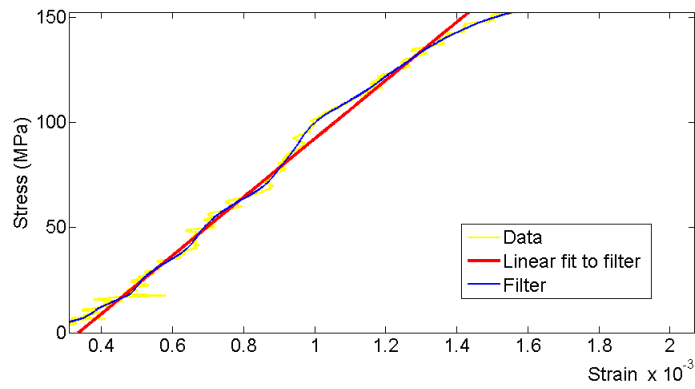
2.5 Stress relaxation test

Stress relaxation tests are performed on the tensile machine. The cross heads are moved until the desired force is applied. Then, the cross heads are stopped and their positions fixed. The relaxation of the force is then measured with the load cell.

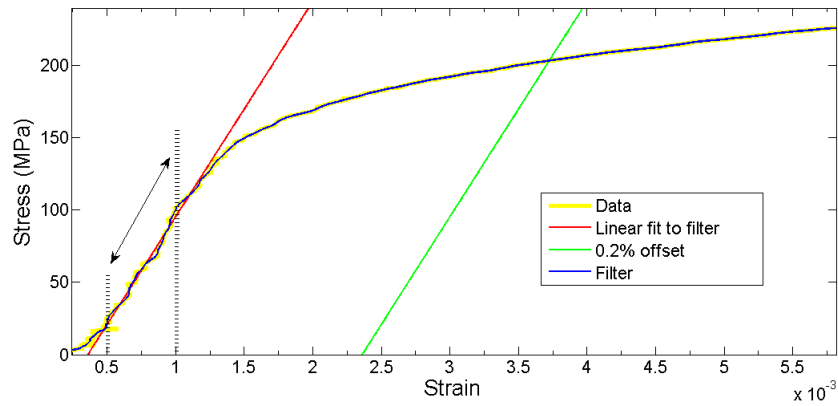
To determine the effect of heat on the deformation of a sample under elastic stress and validate FEM calculations, a bending test has been developed (see Appendix A).



(a)



(b)



(c)

Figure 17: (a) Filter applied to data, (b) fit of first order polynomial to filtered data and (c) plot of the 0.2% offset.

3 Results and Discussion

In this chapter the results of the performed experiments will be shown and discussed. On forehand we know from the steel supplier, that in the as received condition this steel is in the ferritic phase. The precise finishing steps applied by the supplier are not known. It is assumed that the last step in the production of the steel strips is cold rolling to reduce the thickness, as well to introduce a lot of strain in the material to make it stronger. Thereafter the strips are annealed, i.e. heated for some time at $750\text{ }^{\circ}\text{C}$, to relief a part of the stored strain.

3.1 Microstructural analysis

To characterize the material on a microscopic scale, we will look for anisotropy and the effect of a heat treatment on the grain structure.

First, pole figure plots of the material in the as received condition (the reference) and a sample which has been heated 30 minutes at $700\text{ }^{\circ}\text{C}$ are compared. Therefore the samples are rotated such that the normal direction is facing outwards towards the reader and the Rolling- and Transversal Direction (RD and TD) as indicated in figure 18. The pole plots of figure 18(a) show a clear texture visible in the three cubic directions, which is induced in the material by the cold rolling of the steel supplier. After the heat treatment the pole figures are reduced in shape and intensity to some extent (figure 18(b)), but the strong texture is still present: i.e. the grains still have a preferred orientation in the rolling direction.

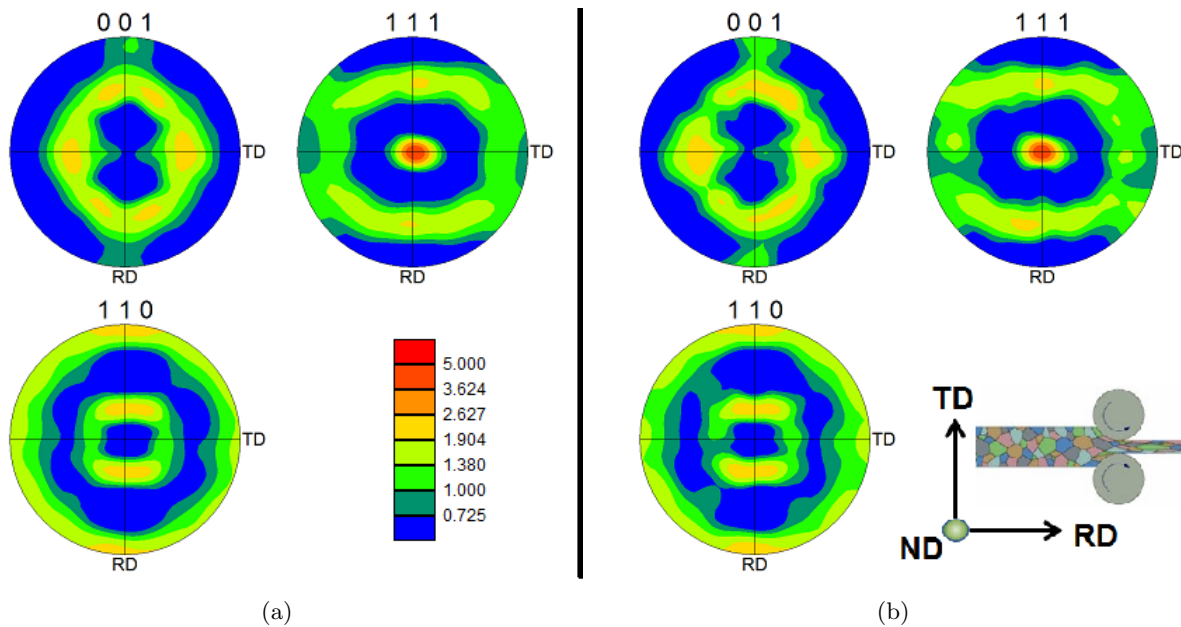


Figure 18: Pole figure plots of (a) the as received (reference) sample and (b) a sample heated 30 minutes at $700\text{ }^{\circ}\text{C}$ and definition of directions [14].

An analysis of the grains is performed for different types of samples: samples heated to $300\text{ }^{\circ}\text{C}$, $500\text{ }^{\circ}\text{C}$ or $700\text{ }^{\circ}\text{C}$ and cooled afterwards before measurement, compared to the as-received (reference) condition.

In figure 19 the inverse pole figures are shown from the material in the as received state (the reference)

and a sample which has been kept at 700 °C for 30 minutes and cooled to room temperature before analysis. Grain boundaries are defined when the misorientation between two scanning points is larger than 5 degrees. All grains are indexed as ferritic.

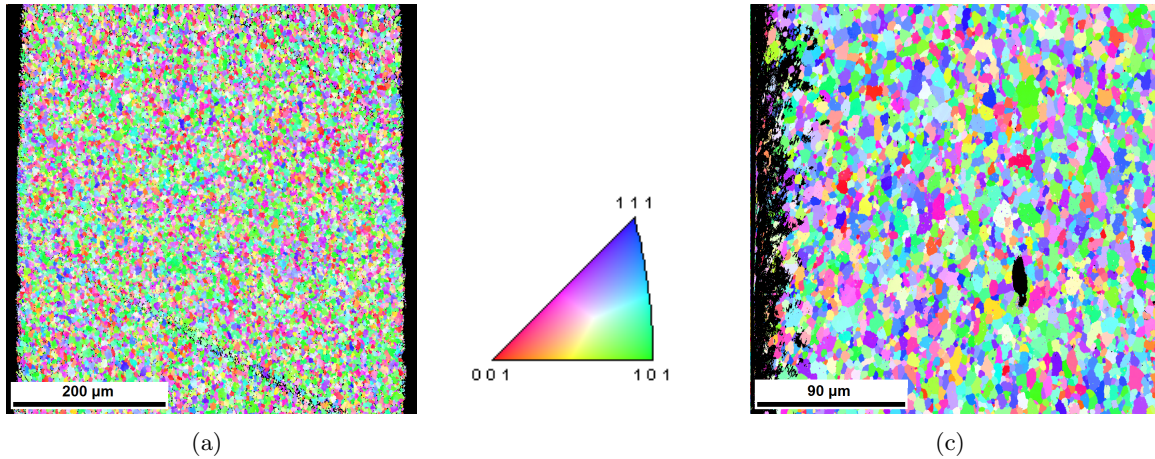
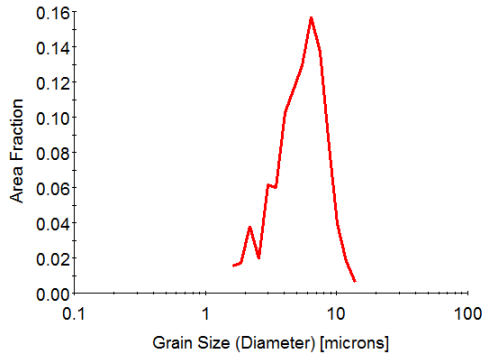
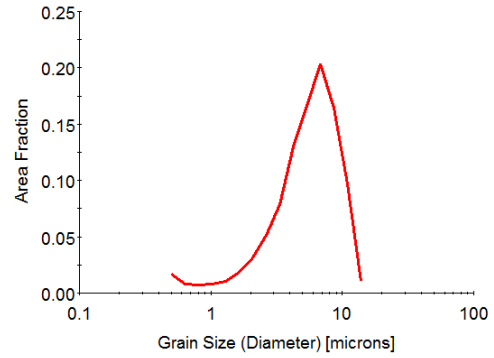


Figure 19: *Inverse pole figures of the material: (a) area of 450 x 450 μm in the as received state, stepsize 1 μm; (b) area of 250 x 250 μm after a heat treatment of 30 minutes at 700 °C, stepsize 0.3 μm.*

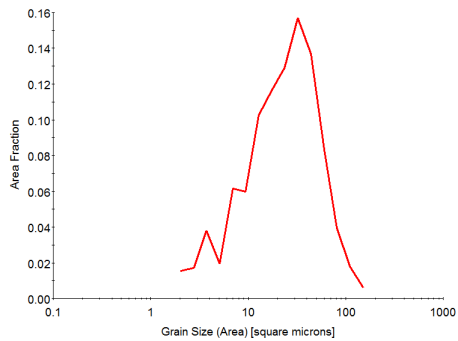
From these samples, the fractions of the grain size area and diameters have been calculated. The peaks of the grain size diameter lie at 6.4 μm and 6.8 μm for the reference and heat treated sample respectively. For the grain size area these values are 32.3 μm² and 36.2 μm². The reference has been scanned with a step size of 1 μm. Since the grains have a diameter of about 6.5 μm, the calculation for this sample could be slightly influenced and grains below 1 μm are not observed. However, the calculated grain size diameter and area of the two samples are very similar. Therefore we conclude that a heat treatment of 700 °C for 30 minutes does not change the grain size significantly.



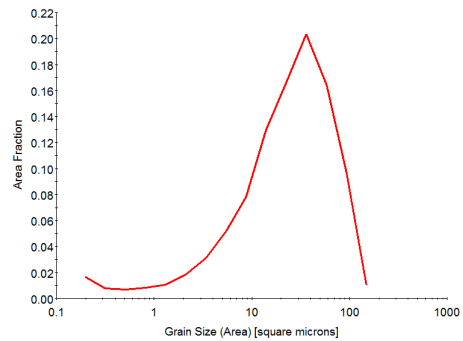
(a) Reference



(b) 30 minutes at 700 °C



(c) Reference



(d) 30 minutes at 700 °C

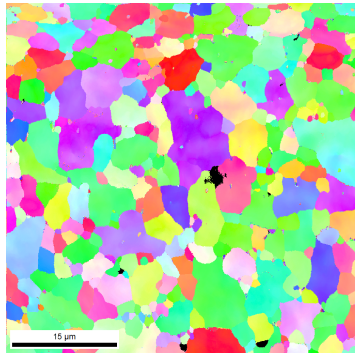
Figure 20: Grain size diameter with (a) peak at $6.5 \mu\text{m}$ and (b) $6.8 \mu\text{m}$. The grain size areas peak at $32.3 \mu\text{m}^2$ and $36.2 \mu\text{m}^2$ for (c) and (d) respectively.

In figure 21, the Image Quality (IQ) and Inverse Pole Figures (IPF) maps of reference and heat treated samples (5 minutes at 300 °C, 500 °C or 700 °C) are shown. In the IPF maps can be seen that the large grains contain smaller grains of about 1 μm . These smaller grains appear as dark spots on the IQ maps, indicating that they have a lower Kikuchi pattern quality than the large grains.

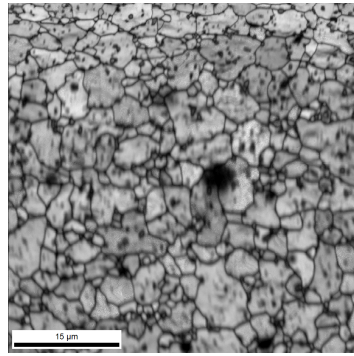
A chemical analysis with EDS has been done on an area containing only a few grains. On the SEM images of figure 22(a), the large grains can be identified, and also circular features of about 1 μm . The long rectangular shapes are remnants from sample preparation. In figure 22(b)-(d) can be seen that the features have a relative low amount of iron, but contain increased amounts of chromium and carbon. The spectrum of one of these features has been quantified in table 4 and confirms a decrease of iron, but an increase in chromium and carbon compared to the overall chemical composition of table 1. Therefore we have identified these features as carbides, which in general could be structures with a relation like $(\text{CrFe})_{23}\text{C}_6$. The solubility of carbon in ferrite is very low: 0.005 wt% at 0 °C, and 0.022 wt% at 727 °C [12]. The carbon can only be present in larger amounts if it is grouped in carbides or at grain boundaries. The latter is not observed in figure 22(d).

Element	Shell	Wt.%	At.%
C	K	3.26	13.18
O	K	0.00	0.00
Cr	L	36.84	34.39
Mn	L	0.86	0.76
Fe	L	58.62	50.94
Si	K	0.42	0.73
Total		100.00	100.00

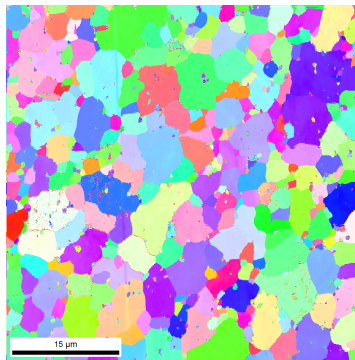
Table 4: *Element configuration of a feature of figure 22.*



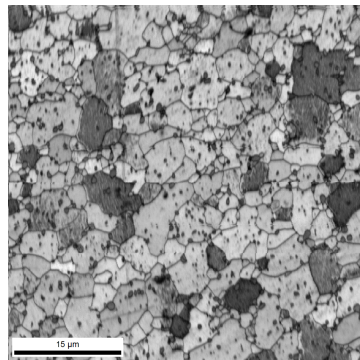
(a) Reference IPF



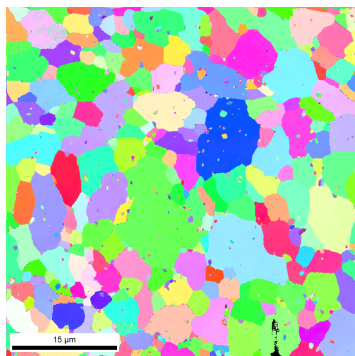
(b) Reference IQ



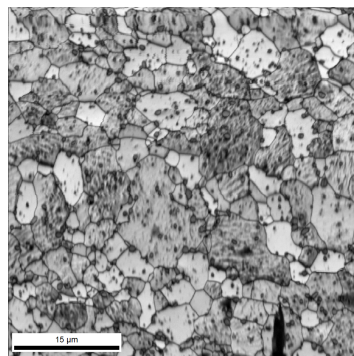
(c) 5 minutes at 300 °C IPF



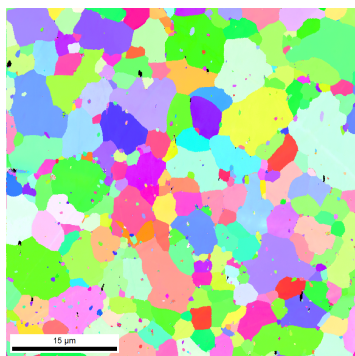
(d) 5 minutes at 300 °C IQ



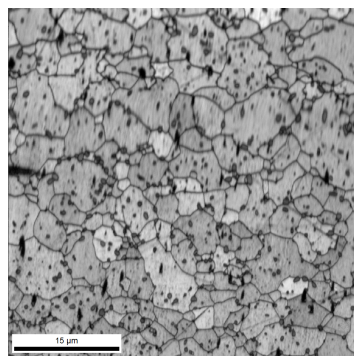
(e) 5 minutes at 500 °C IPF



(f) 5 minutes at 500 °C IQ



(g) 5 minutes at 700 °C IPF



(h) 5 minutes at 700 °C IQ

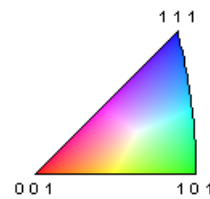


Figure 21: *Image Quality (IQ) and Inverse Pole Figures (IPF) maps of reference and heat treated samples.*

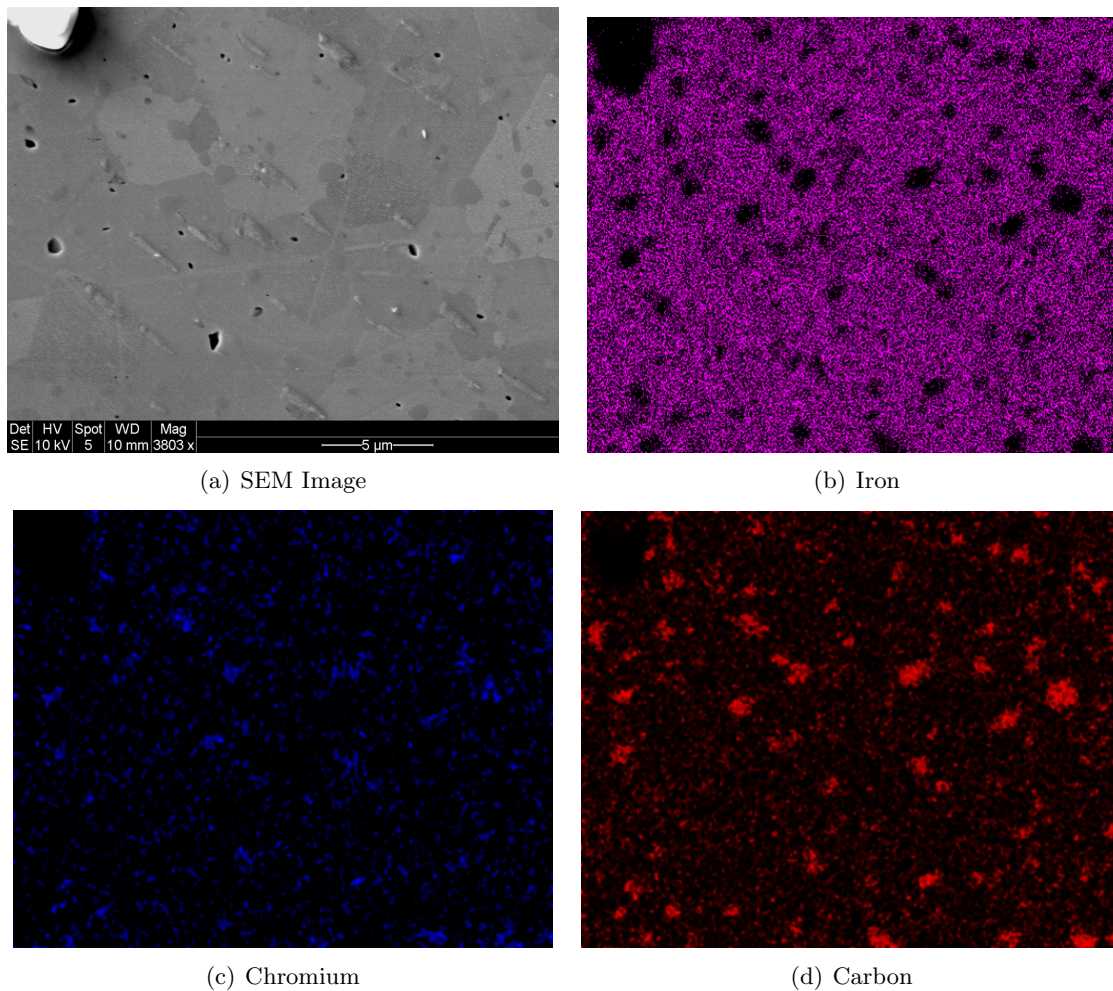


Figure 22: (a) SEM image of the surface and EDS-element mapping of this area for: Iron (b), Chromium (c) and Carbon (d). Bright colors indicate a higher concentration of the elements. The sample has a thickness of 0.5 mm and has been heated at 700 °C for 5 minutes.

The observation that grains do not grow on the considered timescale and temperatures leads to the elimination of the Hall-Petch relation, where flow stress is related to the inverse square root of the grain size diameter, as the underlying process. Therefore we will direct our focus to the distribution of strain inside the grains. The connection and an algorithm for mapping misorientation and plastic deformation using the EBSD technique, was shown by Brewer et al. [15] and later by Kamaya [16–18]. Dislocations are lattice defects which locally change the orientation of the crystals. The strains which are induced by these misorientations can be made visible with the use of the commercial TSL software [19], by determining the Kernel Average Misorientation (KAM). Hereby, the misorientation of each point and all its neighbours is calculated. The average misorientation is the average of the difference in misorientation of the point with each of its six neighbors, as shown in figure 23 (top). When the difference in misorientation exceeds a value of 10° , a boundary is drawn and the neighbors outside the boundary are excluded from the average (figure 23, bottom). The KAM is a good method to show the misorientation gradients. In order to visualize the distribution of misorientations in the grains (an absolute approach), the Grain Reference Orientation Deviation (GROD) method can be used. The basis of GROD is the same as for the KAM. For all points the average misorientation is calculated. Inside each grain, the kernel with the smallest average misorientation is used as a reference. All other points are indexed with the absolute difference of the average misorientation and the reference orientation.

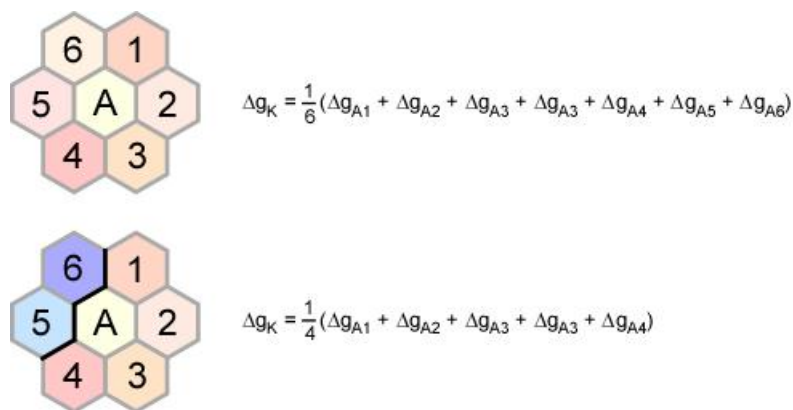
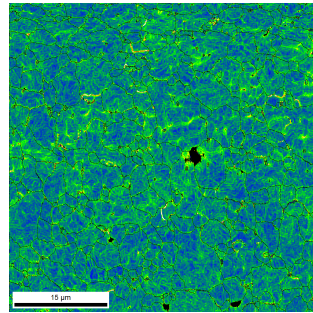


Figure 23: Calculation of the Kernel Average Misorientation [19].

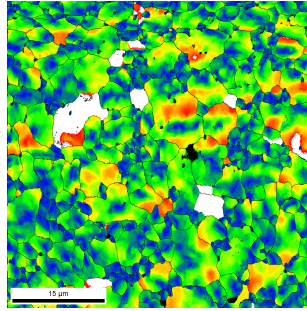
These maps have been made for the same samples as in figure 21 and are shown in figure 24. In order to see the difference between the different samples, the legenda for the KAM ($0-1.5^\circ$) and GROD ($0-4^\circ$) are different. For the reference sample we see a large amount of gradient lines inside the grains, around the carbides and at the grain boundaries. On samples heated at 500°C and 700°C the misorientations have moved from the inside of some grains. Also the concentration at boundaries and carbides is less compared to the reference. The straight lines in figure 24 (c), (d), (g) and (h) are probably scratches which have not completely been removed during sample preparation (also visible on figure 21(f)). The GROD maps show the same trend: in the reference sample the strain is located inside the grains and on triple points. In some grains of the reference sample the carbides are indexed with a low angle. Probably points inside the carbides are taken as the reference point. This might influence the image, but clearly there is strain around carbides and at grain boundaries. The non-indexed (white) points have a value larger than 4° . The scale has been chosen this way, because most points have a low index and differences would not be visible anymore.

The samples heated at 500°C and 700°C show a clear contrast with the reference sample, since most

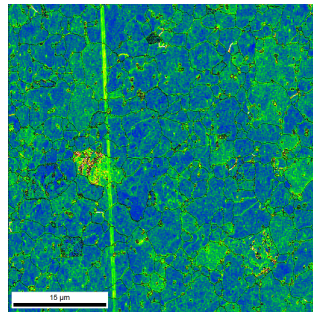
of the strain has been resolved. The sample heated 5 minutes at 300 °C is a transition between the two regimes, with both strain-free and strain containing grains.



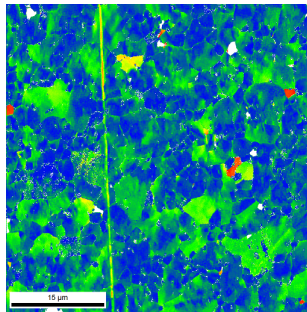
(a) Reference KAM



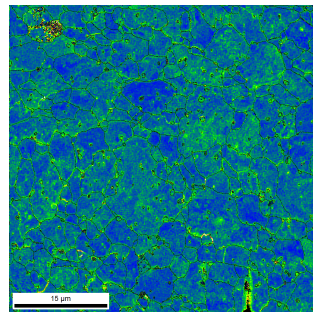
(b) Reference GROD



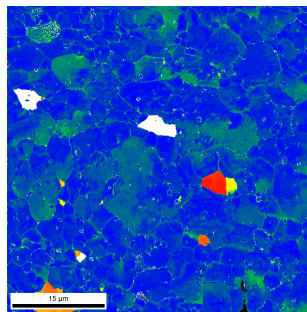
(c) 5 minutes at 300 °C KAM



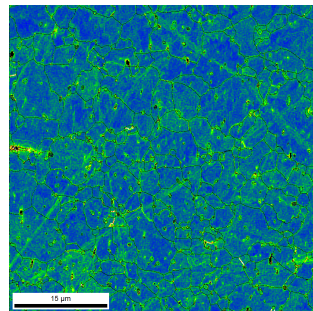
(d) 5 minutes at 300 °C GROD



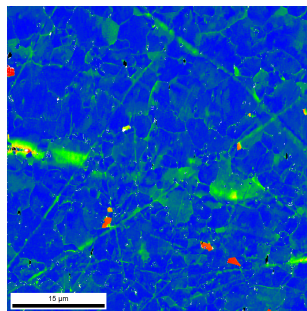
(e) 5 minutes at 500 °C KAM



(f) 5 minutes at 500 °C GROD



(g) 5 minutes at 700 °C KAM



(h) 5 minutes at 700 °C GROD



(i) Legenda KAM



(j) Legenda GROD

Figure 24: *Kernal Average Misorientation (KAM) and Grain Reference Orientation Deviation (GROD) maps of reference (as received) and heat treated samples.*

In a closer look to the KAM map of the reference sample (figure 25), we see that the local misorientations form a cell structure inside the grains. They concentrate around the carbides (dark spots) and extend to other carbides and the grain boundaries. This is part of a recovery process which has been started with a heat treatment by the steel supplier after the dislocation generation process of rolling. When this process is extended by a heat treatment of 5 minutes at 500 °C, the dislocation are thermally activated to climb and glide further towards the formed sub grain structures, grain boundaries and carbides. During these movements, dislocations of opposite sign may annihilate by gliding towards each other. In the maps of figure 24 (e) and (f) we observe grains where only a few misorientations are concentrated around the carbides and grain boundaries, indicating that the as received material further recovers after a short further heat treatment.

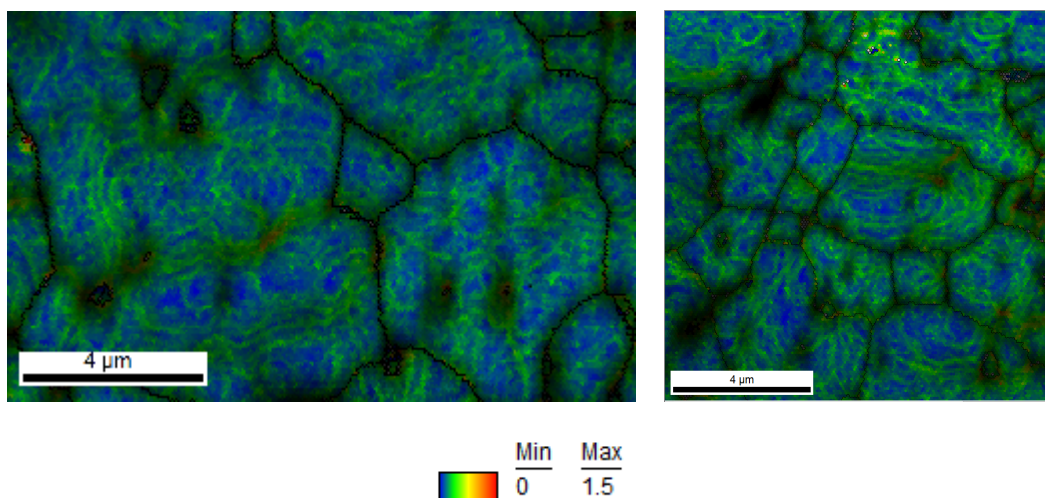


Figure 25: *Combined Image Quality and KAM map of the reference sample.*

The effect of short annealing on tensile characteristics becomes visible in figure 26. Here, 3 samples have undergone a heat treatment of 5 minutes at 700 °C and compared with 3 samples in the as received condition.

In the as received condition the material has a clear drop in stress at the yield point, while the heat treated samples do not show this drop and have a gradual change from elastic to plastic behavior. The stress required for plastic deformation is therefore higher for the as received sample. It is common for bcc metals that a sudden drop in load marks the onset of plastic deformation, since dislocations escape from impurity atmosphere's and become mobile [32]. The obstacles for the moving dislocations can be strong or weak, depending on the angle of bending the dislocations has in its vicinity [34]. A second distinguishment is the force which the obstacle applies on the dislocation line, which can be diffuse or localized forces. Diffuse forces are distributed uniformly over a long length (after Nabarro), whereas strong forces bend the dislocation line to follow a contour of minimum interaction energy between obstacles, while line tension prevents bending at large angles for weak obstacles. In the Friedel relation, localized forces exert on a small part of the line. Therefore the dislocation can bow with a certain radius between the dislocation line, depending on the strength of the obstacle. The impurity (or Cottrell) atmospheres are strain fields caused by (self) interstitials like carbon, which distort the lattice. It was explained by Cottrell [33] that these fields can be relaxed through diffusion of the (self) interstitial towards a dislocations. In certain configurations, they pin the dislocations and suppress their

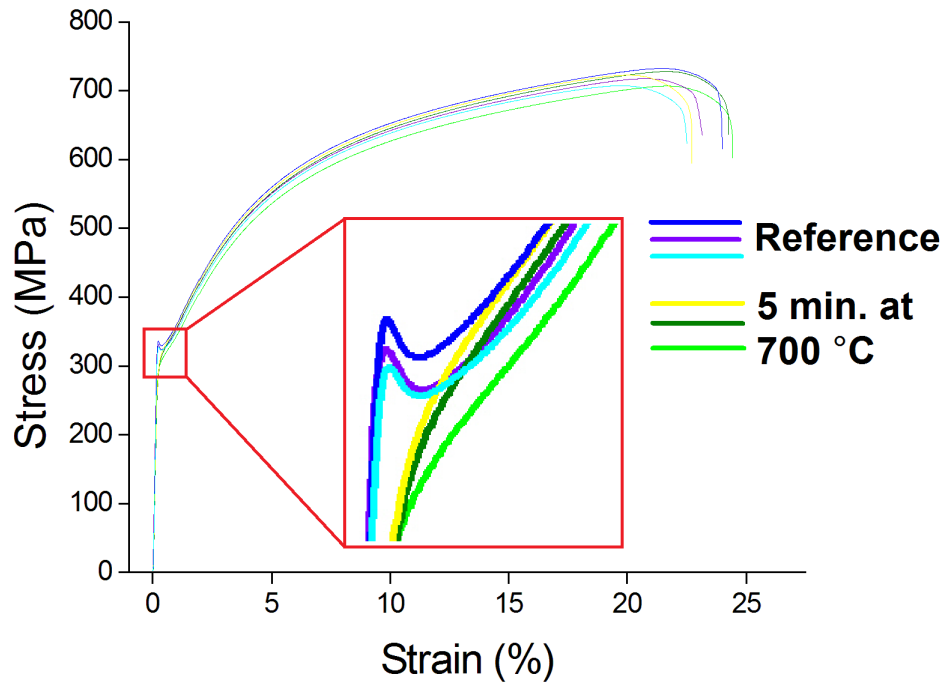


Figure 26: Yield point characteristics of the reference compared to samples with a heat treatment of 5 minutes at 700 °C.

mobility. When the applied stress becomes locally strong enough, the dislocations break free from the impurity spheres: the yield drops. It was estimated that the pinning barrier is very high (about a tenth of the elastic modulus), but also very narrow and can therefore be overcome by thermal fluctuations. At higher temperatures the thermal fluctuations can unpin some dislocations, creating a small surface from where the applied stress can free the barriers of other pinned dislocations. When the material comes to rest, the dislocations can be attracted to the impurities and become pinned again. The as received samples have a drop at the yield point of about 10 MPa, while the drop is not present anymore for the further heat treated samples, indicating that for the latter the dislocations are probably unpinned.

3.2 Transformation characteristics

In this section, the influence of anisotropy on phase changes and the thermal expansion will be discussed.

The phase diagram for iron-chromium-carbon at 13 % chromium is shown in figure 27. N004, with 0.32 % carbon, is a mixture of ferrite (BCC α -iron) and carbides at room temperature [2]. Carbides in this steel are local structures of $(CrFe)_{23}C_6$.

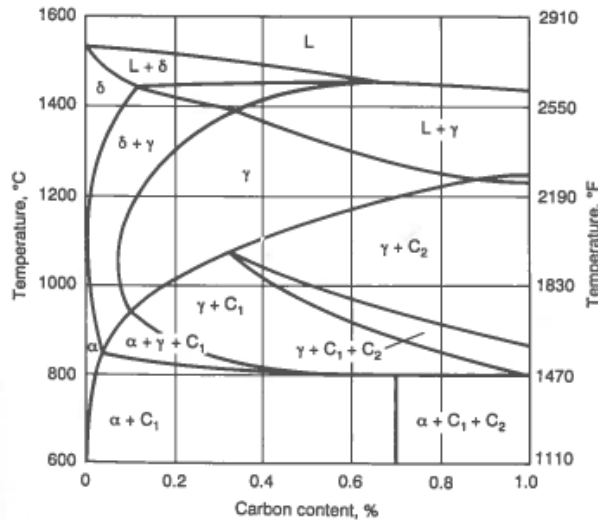


Figure 27: Phase diagram for iron-chromium-carbon at 13 % chromium [2].

Between 850 °C and 1080 °C, the ferrite transforms to austenite (FCC γ -iron). By cooling down, a more complex path is followed. This is shown with a continuous cooling transformation (CCT) phase diagram in figure 28. Here, austenite at 980 °C is cooled with a continuous (temperature) rate. This rate is crucial for the final structure and determines when and how much martensite will be formed. Martensite is a form of ferrite, but has more strength. In the austenite phase, carbon (from the carbides) is dissolved in the crystal structure. Ferrite with its BCC structure in principle can not hold the same amount of carbon in its crystal structure. By fast cooling however, the carbon cannot diffuse out of the crystal structure during the phase transformation from austenite to martensite and becomes trapped. The new structure is supersaturated with carbon and much stronger and harder than ferrite. The martensite crystal has a BCT-structure which is very similar to ferrite, but has one extended side due to the additional carbon in the crystal (figure 29). The stretched crystal structure causes a volume change, and tension inside the grains. Often the martensite is annealed for a short time to relief an amount of this tension. During the annealing a part of the trapped carbon is released.

This cycle is of extreme importance to the hardening of the shaver caps. There will be volume changes due to heating, cooling and phase transformations. To show this effect, a dilatometer test has been performed ¹. A full heating and cooling cycle with a temperature rate of 10 °C/min has been performed. The relative length change as a function of temperature is shown in figure 30. Up to 809 °C the sample expands and has a constant expansion coefficient. The derived values in figure 31 agree with the

¹Acknowledgments to Dr. Kornell CSACH, Institute of Experimental Physics, Kosice, Slovakia, for developing the sample preparation technique and performing all dilatometer tests presented in this work.

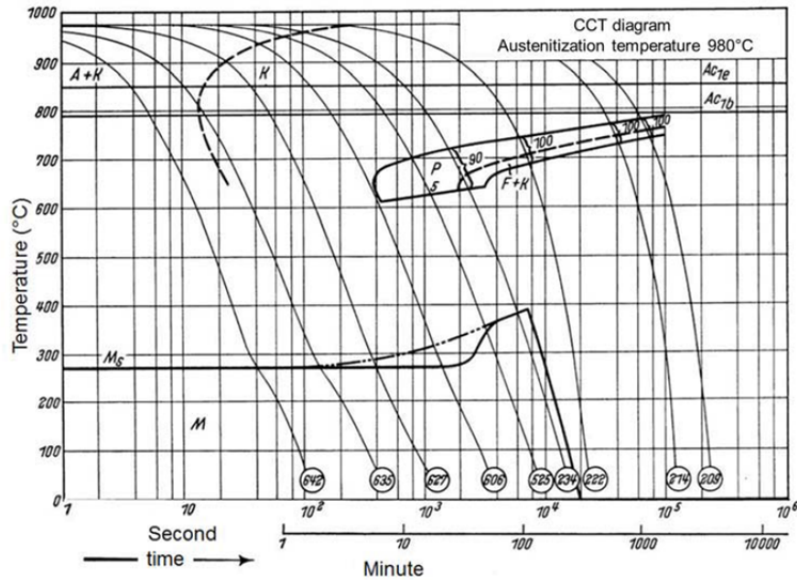


Figure 28: Continuous cooling transformation (CCT) phase diagram [35].

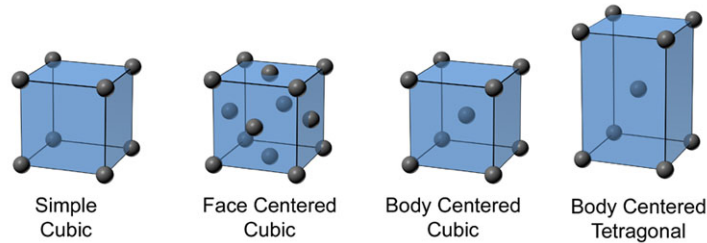


Figure 29: Crystal lattices [13].

standard values of $10.3 \times 10^{-6}/^{\circ}\text{C}$ for $0 - 100^{\circ}\text{C}$ and $11.7 \times 10^{-6}/^{\circ}\text{C}$ for $0 - 500^{\circ}\text{C}$ [21]. Between 809°C and 841°C a relative large change in volume occurs. 809°C is the starting of the phase transformation of ferrite (BCC structure) to austenite (FCC structure). After the sample is kept at 950°C for 10 minutes, it is fully austenitized and most of the carbides are solute in austenite. Then cooling with $10^{\circ}\text{C}/\text{min}$ is started and slowly carbides are formed again. When a temperature of 713°C is reached, the austenite is partly transformed to perlite. Transformation to martensite starts at 381°C . This is well in agreement with figure 28, the cooling rate of $10^{\circ}\text{C}/\text{min}$ is in between lines 525 and 234 as well as the starting temperatures for transformation. The forming of perlite microstructures can be avoided by cooling with a rate higher then 35 degrees/minute. With this rate, there will only be formation of martensite at a starting temperature of about 300°C , as can be seen in figure 28 represented by line 606. The theoretical route with phase changes for the shaver caps is illustrated in figure 32.

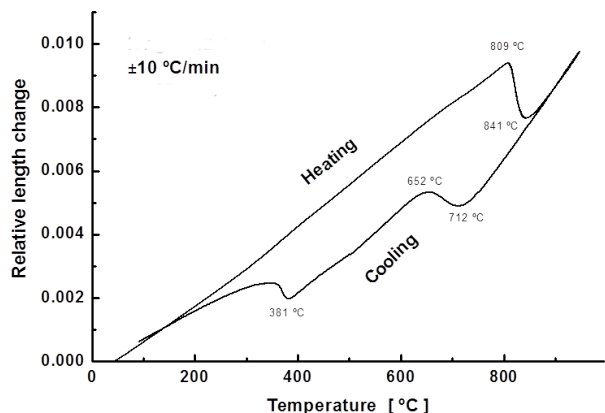


Figure 30: Dilatometer measurement of a full heating and cooling run on a 0.45 mm thick sample with length of 12.4 mm.

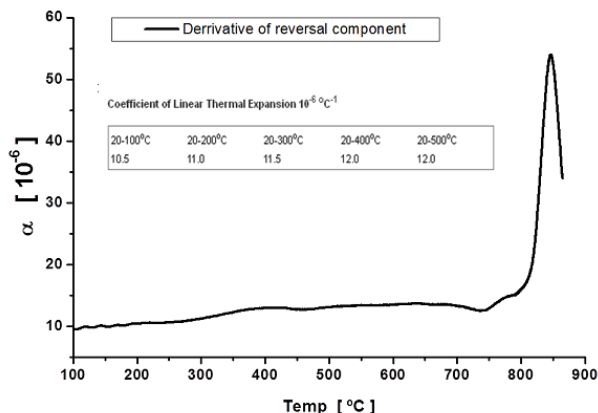


Figure 31: Temperature dependence of coefficient of thermal expansion.



Figure 32: Theoretical temperatures of start phase changes.

The effect of cooling rate on the avoiding of perlite is shown in figure 33. The cooling rate as displayed in the graph is maintained to 450 °C, thereafter the rate is not well controlled. For rates higher than 50 °C/min the perlite nose of figure 28 is avoided and only martensite will be formed.

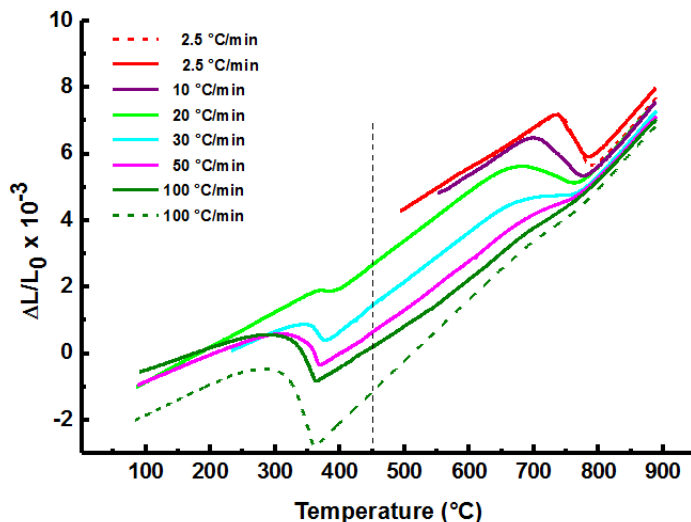


Figure 33: The effect of cooling rate on the avoiding of perlite. Cooling rates are maintained to 450 °C, indicated by the dotted vertical line.

For anisotropy, four samples in the rolling direction (denoted as parallel) and three in the transversal direction (perpendicular) are compared (figure 34(a)). They are heated with 5 °C/min to 900 °C, with a (constant) modulation of ± 3 °C. Therefore, the change in length can be divided in a reversible and irreversible part (figure 34(b) and (c)). The spread in the Overall picture is caused by irreversible processes (which start to become visible at 400 °C), since both parallel and perpendicular samples have the same reversible behavior.

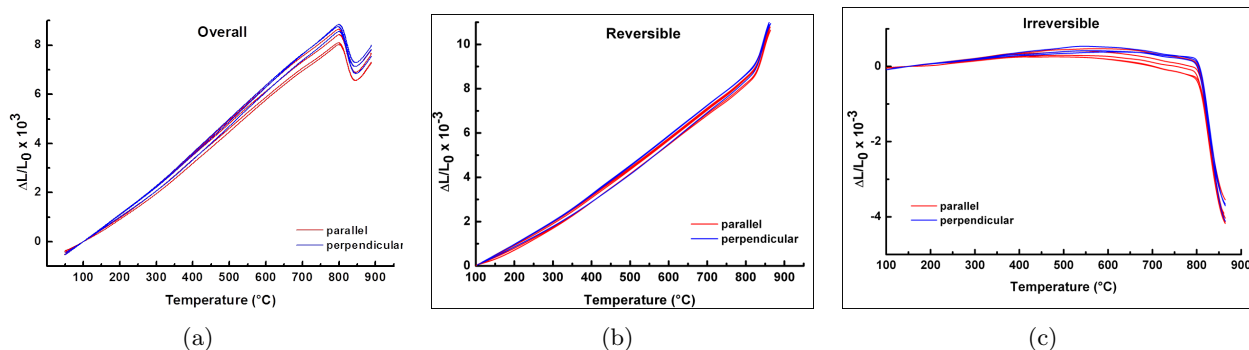


Figure 34: Dillation (a) split in reversible (b) and irreversible part (c).

The relative length changes at the start of austenization (the top at 800 °C and bottom at 840 °C) are measured and shown in table 5. There is a spread in all samples, which could be due to small fluctuations in the coil where the samples are cutted from, but the samples in the transversal direction seem to have a larger overall extension at the start of austenitization.

Direction sample	Top ($\times 10^{-3}$)	Bottom ($\times 10^{-3}$)	Volume change (%)
parallel (RD)	8.09	6.57	0.152
parallel (RD)	8.43	6.90	0.153
parallel (RD)	8.65	7.14	0.151
parallel (RD)	8.02	6.57	0.145
perpendicular (TD)	8.55	6.86	0.169
perpendicular (TD)	8.75	7.13	0.162
perpendicular (TD)	8.85	7.30	0.155

Table 5: Volume change at the start of austenitization of parallel and perpendicular samples.

3.3 Mechanical properties

Various tensile test have been performed to investigate the influence of temperature and anisotropy on the mechanical properties.

Room temperature

The results of the comparison of samples from the two coils (thickness 0.3 and 0.5 mm) are shown in table 6. The flow stress and E-modulus have been determined according to the method described in Chapter 2.

Specimen nr.	E-modulus (GPa)	Flow stress (MPa)	Sample thickness (mm)
1	202.4	324.7	0.5
2	205	324.7	0.5
3	200.4	325.1	0.5
4	205.6	323.3	0.5
5	207.7	329.8	0.5
6	207	330.3	0.5
7	215.7	369.3	0.3
8	215.8	367.9	0.3
9	210.4	369.5	0.3
10	215.7	369.7	0.3

Table 6: *E-modulus and flow stress at room temperature of 0.5 and 0.3 mm thick material with $\dot{\epsilon} = 0.012 \text{ s}^{-1}$.*

From these measurements we can deduce values at room temperature of 204 ± 3 GPa and 214 ± 2 GPa for the E-modulus and 327 ± 4 MPa and 369 ± 2 MPa for the flow stress of the 0.5 and 0.3 mm thick samples respectively. The E-modulus of the 0.5 mm thick coil agrees to the standard value of $E = 200$ GPa for AISI 420 in the annealed condition [21]. The yield point is highly dependent on the alloy chemical composition and the annealing time and rate after rolling. Therefore these values can not be compared to standards.

The following series are performed on tensile bars which were cut out in different directions: parallel to the rolling direction (RD), perpendicular to the RD, i.e. the transverse direction (TD) and in between (45°). E-moduli (table 7) are: RD 204 ± 3 , TD 224 ± 2 , 45° 227 ± 1 GPa. Anisotropic behavior is clearly visible in the E-modulus and can be 20 GPa higher in the TD and 45° direction, compared to the RD. Only minor differences in the flow stress between RD and TD are observed.

Specimen nr.	Direction	E-modulus (GPa)	Flow stress (MPa)
1	RD	202,4	324,7
2	RD	205	324,7
3	RD	200,4	325,1
4	RD	205,6	323,3
5	RD	207,7	329,8
6	RD	207	330,3
Average	RD	204,7	326,3
11	TD	226,8	329,3
12	TD	227,1	329,1
13	TD	224,3	328,6
14	TD	224,9	329,8
15	TD	221,8	330,1
16	TD	223,8	330,5
17	TD	222,4	330,9
Average	TD	224,4	329,8
18	45 °	228,7	No data
19	45 °	226,9	Nd
20	45 °	225,3	Nd
21	45 °	226,8	Nd
22	45 °	226,2	Nd
23	45 °	228,6	Nd
Average	45 °	227,1	

Table 7: *E*-modulus and flow stress at room temperature of 0.5 mm thick material with $\dot{\epsilon} = 0.012 \text{ s}^{-1}$, in Rolling-, Transverse- and 45 degree Direction.

Elevated temperature

The effect of temperature on the mechanical properties is shown in figure 35, for the range 20 °C to 900 °C.

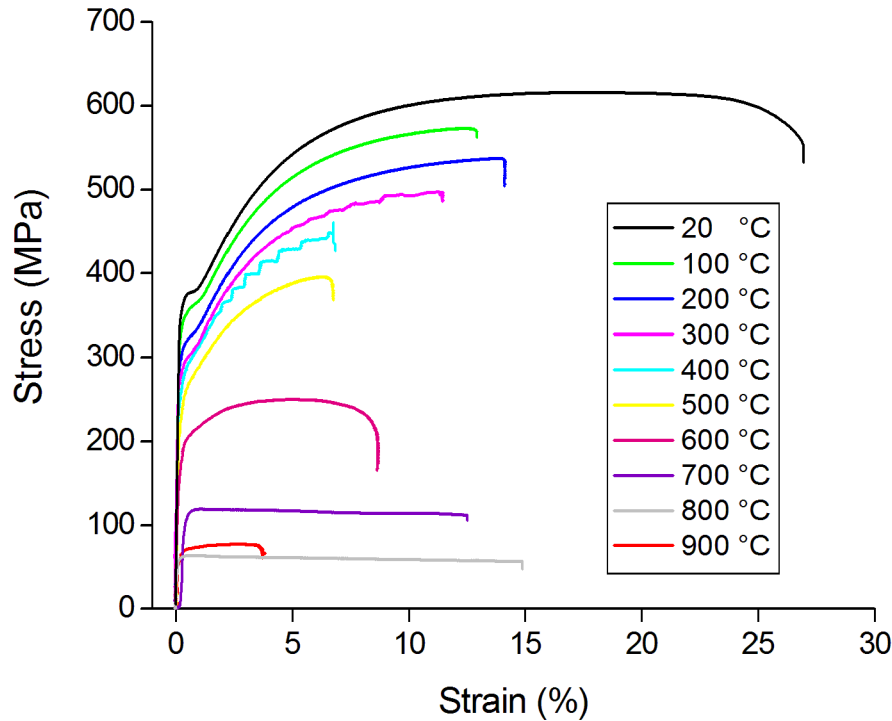


Figure 35: True stress - true strain diagram of tensile test at elevated temperatures of 0.3 mm thick material with $\dot{\epsilon} = 0.012 \text{ s}^{-1}$. The behavior of the material changes at elevated temperatures. For comparison and illustration of the different behavior, the curves are not cut off at the onset of necking.

It is clear that strength decreases with increasing temperature, with a large drop between 500 °C and 600 °C. After 600 °C, the material hardly recovers (there is no strain-induced hardening) and yields to fracture. Hardening appears as from the moment that plastic deformation occurs, dislocations multiply (by Frank-Read sources) and interact with each other and with barriers whereupon their motion is reduced [8]. An increase in temperature lowers the energy required for dislocations to overcome these barriers. At a certain temperature, the required energy is too low for the barriers to constrain the motion of the dislocations. They move uninhibited through the grains, and do not pile up at pinning points, so the material can not recover. A microscopic investigation of the fractured surface, shown in figure 36, illustrates this change.

At room temperature the fractured surface is about 125 μm wide and shows a rough surface with sharp voids. At 600 °C this surface is 40 μm , and at 900 °C only 2 μm wide. Since the original thickness of the specimen was 0.3 mm, the effect of necking has become visible here. With increasing temperature the metals becomes more ductile and the area of fracture surface decreases enormous at 900 °C. At this temperature the metal has become very ductile. As can be seen in figure 36(d) and 36(c), the fracture surface has only voids on one thin ridge of 2 μm and the failure can be classified as rupture. Ductility

allows the material to redistribute localized stresses by void coalescence, while brittle materials build up localized stresses. If a crack is formed in this case, it will spread rapidly over the section and cause a sudden fracture. At room temperature the central crack propagates through narrow bands of high shear strain at angles of 60° [8], as seen in figure 37(a), and (micro-) voids nucleate in these shear bands. Higher temperatures can cause the micro-voids to grow and coalescence can occur. This allows the central crack to propagate with a zig-zag movement as seen in figure 37(b), as the number of available slip systems increase.

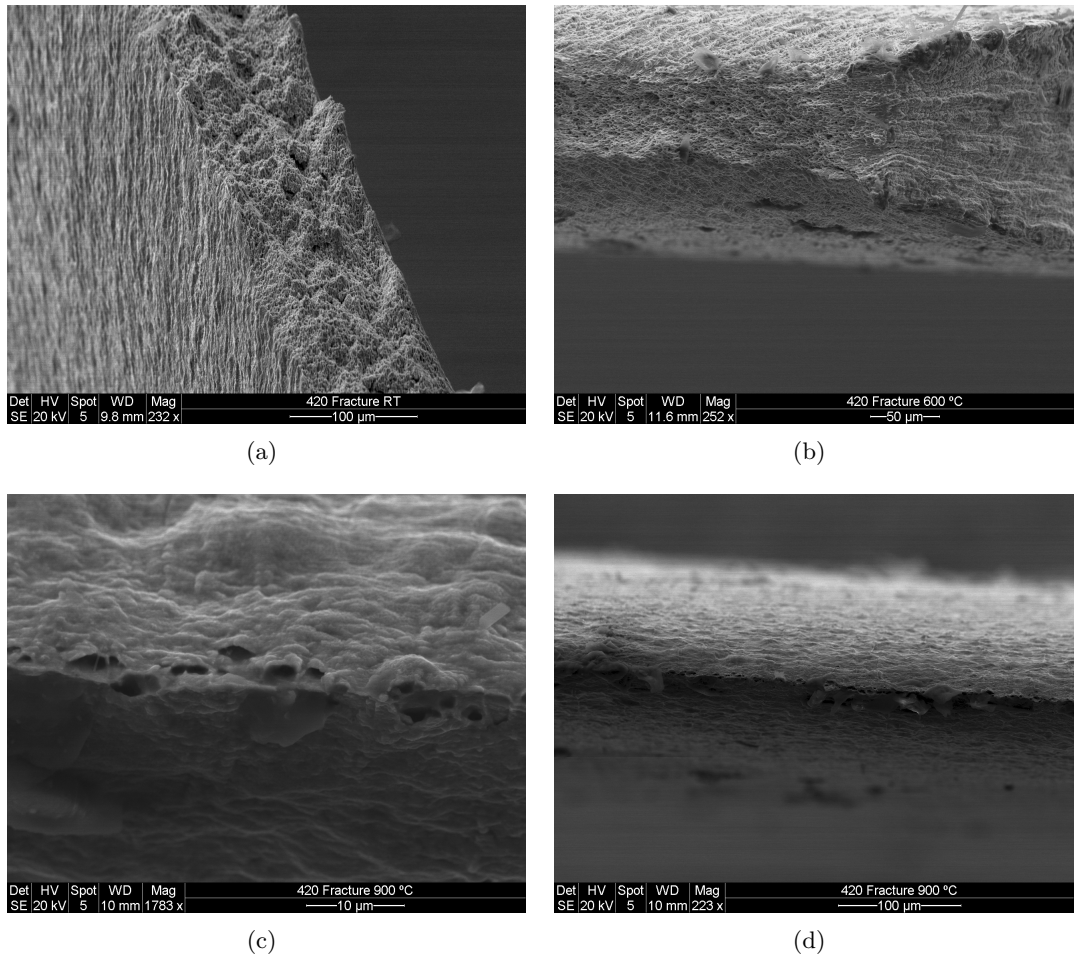


Figure 36: *Top view of tensile fractured surfaces of (a) room temperature, (b) 600°C and (c) 900°C . (d): side view of 900°C .*

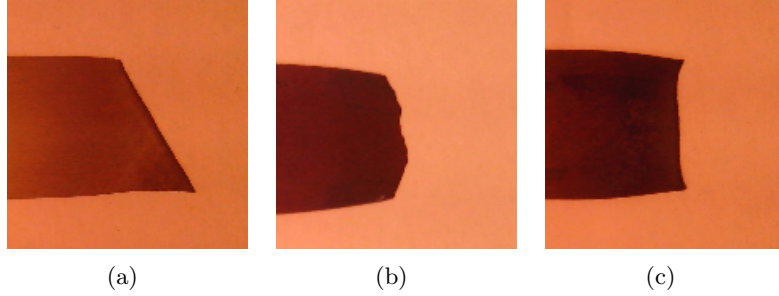


Figure 37: *Fractured tensile bar of tensile test performed at (a) room temperature, (b) 600 °C and (c) 900 °C.*

The start of plastic deformation (yield point) is an important parameter in modeling. The flow stress ($\sigma_{0.2}$) has been obtained from the stress-strain curves of figure 35 and plotted as function of temperature in figure 38(a). The flow stress decreases as temperature increase until 800 °C, where phase transformation to austenite starts. According to Hall [26], who investigated NiCrFe alloys, there is an athermal temperature with a corresponding athermal stress. Below the athermal temperature, the creep system is expected to be dominated by thermally glide of dislocations. In figure 38(b) the athermal temperature has been indicated at 400 °C and the corresponding athermal (or threshold) stress at 279 MPa. The flow stress is not normalized with the E-modulus, therefore this point could be shifted. Above this temperature it is expected that creep is controlled by diffusion.

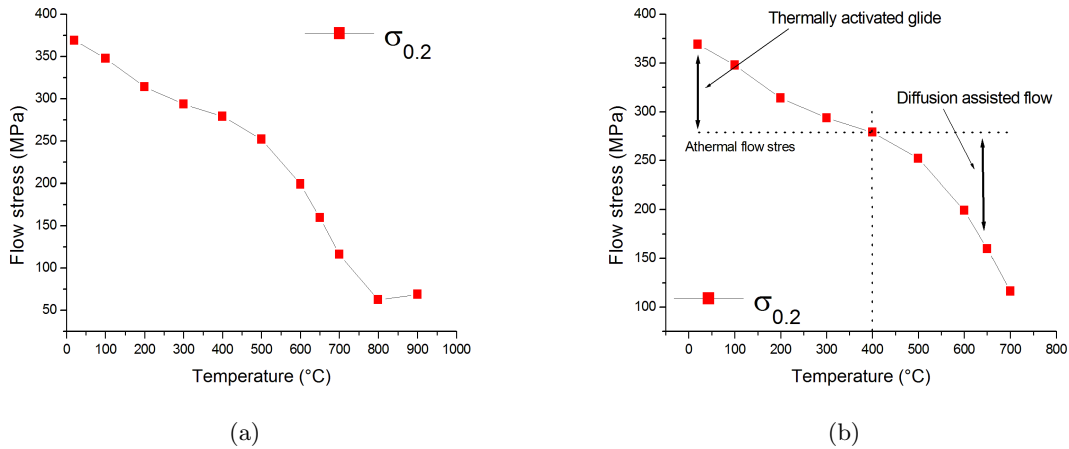


Figure 38: (a) *Effect of elevated temperature on the yield stress of 0.3 mm thick samples, (b) indication of athermal flow stress at 400 °C.*

The elastic modulus has been determined from 40 tensile test samples, at different temperatures and strain rates. Since the E-modulus does not change with strain rate, they have been plotted together in figure 39, where their values are normalized to the E-modulus at room temperature. To indicate the reproducibility of this method of E-modulus determination, tests with one sample in a range of 450 °C to 750 °C have been done. The numerous results between 500 °C and 700 °C show a large spread in the E-modulus for these temperatures. Based on table 6, minor differences in the order of 4 GPa (= 0.02 normalized) were expected due to fluctuations in the material. Further deviations of 10 GPa (= 0.05

normalized) sometimes result from difficulties in finding a relative straight domain on the tensile curve to fit the linear line representing the elastic modulus.

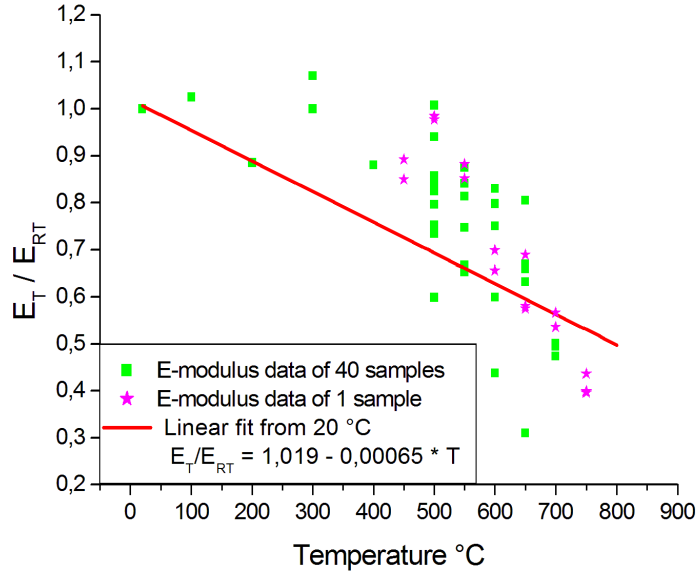


Figure 39: *E*-modulus data normalized to room temperature and proposed linear fit starting at 1 for room temperature.

Chen et al. [28] show in their results for High strength steel (0.16 % C) and Mild steel (0.22 % C) a gradually decreasing *E*-modulus, with an increase in the slope starting at about 500 °C (figure 40(a)). Fukuhara and Sanpei [29] present a more or less constant decrease for a ferritic 0.11 % C steel (figure 40(b)). More graphs of the *E*-modulus as a function of temperature for different types of steel and the effect of the amount of chromium, can be found at [30, 31]. Our results may suggest an S-curve temperature dependence like the results of Chen, but due to the large spread in the data this picture could be misleading. Elastic deformation involves stretching of the bonds. The thermal expansion is given by:

$$\frac{\Delta L}{L} = \alpha \Delta T, \quad (14)$$

with α the coefficient of linear thermal expansion. The *E*-modulus is the second derivative of the potential curve with respect to the interatomic distance. With increasing temperature, the potential of the bonds is lowered but is assumed to hold the same shape. Since the structure (grain size) does not change, we do not expect a large deviation of the gradual change of the potential. Also, as seen in Chapter 3.2, α is constant in the range 0 °C - 800 °C. Therefore we propose a linear decrease of the *E*-modulus with increasing temperature:

$$\frac{E_T}{E_{RT}} = 1.019 - 0.00065 * T, \quad (15)$$

so the *E*-modulus becomes

$$E(T) = 200 * (1.019 - 0.00065 * T), \quad (16)$$

with *T* in °C and *E*(*T*) in GPa.

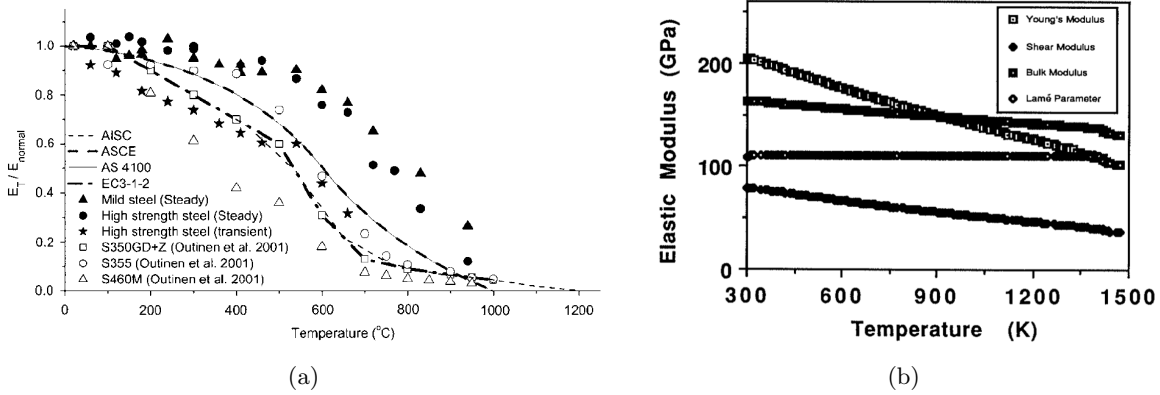


Figure 40: E -modulus dependence on temperature with (a): High strength steel (0.16 % C) and Mild steel (0.22 % C) [28], (b): ferritic 0.11 % C steel [29].

In figure 41 normalized values for the flow stress are plotted together with the data of the E -modulus and the proposed equation. We see that the flow stress follows the line of the E -modulus very close up to 500 $^{\circ}C$. The flow stress decreases faster than the proposed E -modulus above 500 $^{\circ}C$.

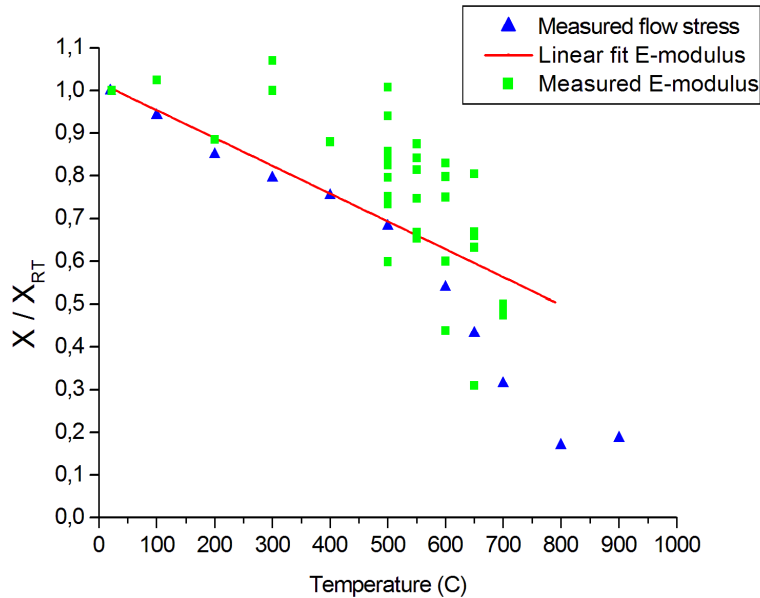


Figure 41: Normalized values of the flow stress and E -modulus with a linear fit applied to the data of the E -modulus.

The drop of the yield stress with increasing temperature could be caused by diffusion in the grains. Carbon (in the crystal lattice) acts as a pinning point for dislocations. The diffusivity, D , of carbon in (α) iron is $3.3 \times 10^{-10} cm/s$ at 300 $^{\circ}C$ and $5.2 \times 10^{-9} cm/s$ at 400 $^{\circ}C$ [27]. The two-dimensional diffusion length, l_0 is defined as:

$$l_0 = \sqrt{2 t D} \quad (17)$$

For the time ($t = 5$ minutes) the tensile bars have been at these temperatures, the diffusion lengths are $4.5 \mu m$ at $300^\circ C$ and $17.6 \mu m$ at $400^\circ C$. Around these temperatures, the carbon in the crystal lattice can diffuse to carbides and grain boundaries, since the grains have an average diameter of about $7 \mu m$. The self diffusion of α -Fe is very low, in the order of $10^{-11} cm^2/sec$ at $700^\circ C$ [20] and is therefore probably not the rate controlling process.

Another indication that the internal structure changes after a heat treatment, is shown by the E-modulus values in table 8. Here the values of E-modulus of samples, which have been heated 5 minutes at $700^\circ C$ and cooled afterwards, are compared to measurements conducted at room temperature and $700^\circ C$. The annealed samples (cooled before measurements) have values of the E-modulus which are about 20 GPa lower than (reference) room temperature samples.

Specimen number	Temperature	E-modulus (GPa)
1-6	Reference	204 ± 3
24	5 min. at $700^\circ C$	180,5
25	5 min. at $700^\circ C$	179,1
26	5 min. at $700^\circ C$	193,7
27	$700^\circ C$	100,2
28	$700^\circ C$	94,8
29	$700^\circ C$	99

Table 8: *E-moduli of samples measured at $700^\circ C$ and after 5 minutes heating at $700^\circ C$.*

Creep

As described in section 2.4.3, material loaded with a force above the yield stress will deform plastically. A load which induces a stress lower than the yield stress should deform the material only elastically. However, when the material is at a certain temperature, plastic deformation can occur even when the stress is lower than the yield stress. This process is called creep and has under a constant load a time-dependent character with three stages, as shown in figure 42.

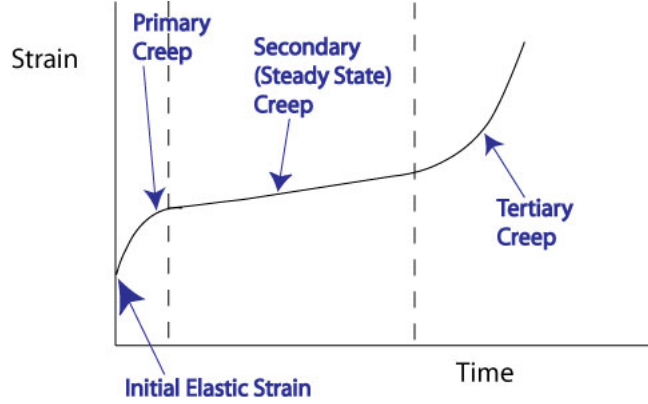


Figure 42: *The three stages of creep during loading under a constant stress [22].*

The results of creep tests at three temperatures are plotted in figure 43. Variations in load show at all temperatures the same effect: an increase of the constant load induces a higher strain rate. Also at higher temperatures the load needed to establish the same creep rate, is lower than at lower temperature (e.g. 75 MPa at 600 °C for $\dot{\epsilon} = 5.0 \times 10^{-7}$ versus 30 MPa at 700 °C for $\dot{\epsilon} = 6.8 \times 10^{-7}$). All curves have the same shape (primary and secondary creep) as the line of 200 MPa at 500 °C. Due to the larger strains at higher temperature, the strain due to primary creep part is relative small compared to the secondary creep strain. Exception is the load of 75 MPa at 700 °C. Here tertiary creep has started after about 20 minutes and the steady state creep rate has been determined from the part before the start of tertiary creep.

Strain-rate $\dot{\epsilon}$, or deformation velocity, is the rate of change in strain of a material with respect to time.

$$\dot{\epsilon} = \frac{d\epsilon}{dt} \quad (18)$$

The creep process is thermally activated and the creep rate can be described by an Arrhenius type equation [24]

$$\dot{\epsilon} = K e^{-\frac{Q_c}{RT}}, \quad (19)$$

where K is a constant for a given stress and strain and might have a dependence of temperature. Q_c is the activation energy for creep, R the gas constant and T the absolute temperature. When dislocations climb or the motion of jogged screw dislocations control the creep motion, it is expected that the steady state creep rate is proportional to the diffusion of atoms

$$\dot{\epsilon} = KDf(\sigma), \quad (20)$$

where $D = D_0 e^{-\frac{Q_c}{RT}}$. In [24] a phenomenological equation is stated, showing the dependence of these two parameters in alloys:

$$\dot{\epsilon} = K e^{-\frac{Q_c}{RT}} \sigma^n \quad (21)$$

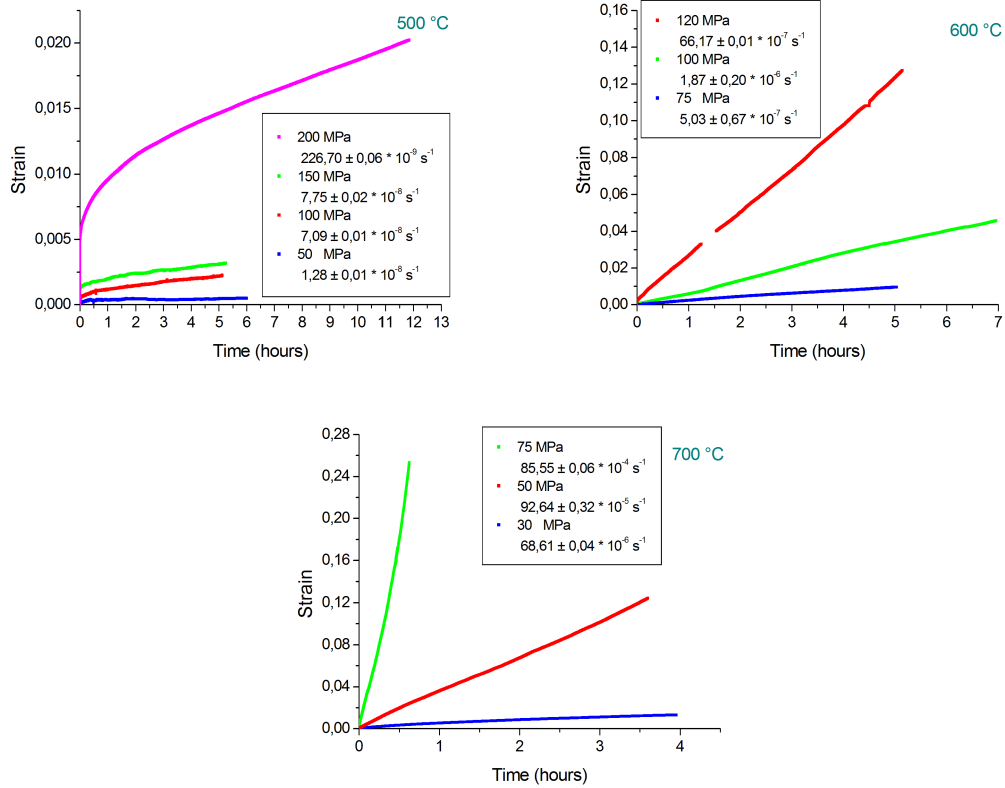


Figure 43: Time vs. strain for constant loading at three temperatures. Calculated strain rate from the slope is indicated.

The parameters of this equation will be calibrated in Chapter 4.

Strain rate effect

Consequence of equation 21: stress is a function of temperature and strain rate. To investigate this dependence, tensile tests at various strain rates and temperatures have been performed according to table 9.

Temperature (°C)	Strain rates (s^{-1})
500	$10^{-2}, 10^{-3}, 10^{-4}$
550	$10^{-2}, 10^{-3}, 10^{-4}$
600	$10^{-2}, 10^{-3}, 10^{-4}$
650	$10^{-2}, 10^{-3}, 10^{-4}$
700	$10^{-2}, 10^{-3}, 10^{-4}$

Table 9: Measured strain rates and temperatures.

The results of three temperatures are plotted in figure 44. Some tensile test were aborted after a certain strain level due to the time of the measurement or because some markers exceeded the range of the LEX. However, the measured range for all curves is sufficient to determine the flow stress and the trend of strain hardening. For all temperatures the flow stress increases with increasing strain rate. This effect

is more pronounced at 600 °C and 700 °C than for 500 °C, where the difference is relatively small. At 600 °C there is still some strain hardening, while for 700 °C this effect is nearly absent. This confirms, together with the creep results of figure 43, that in the temperature region 500 °C - 700 °C a change in internal processes occurs.

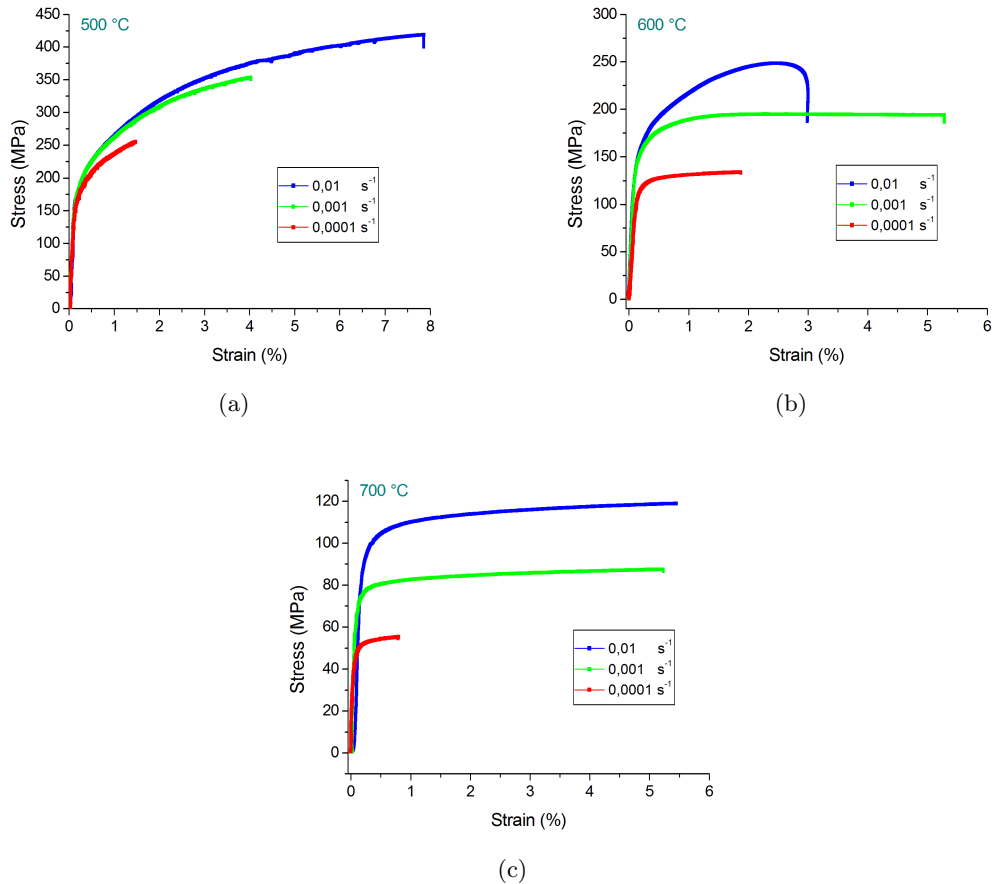


Figure 44: 3 strain rates for temperatures: (a) 500 °C, (b) 600 °C and (c) 700 °C.

The stress exponent n has been determined for the creep and the tensile data and is shown in figure 45 (derivation of this exponent will be done in Chapter 4). The stress exponent is the inverse of the strain rate sensitivity, i.e. a low value of n means a high strain rate sensitivity. The tensile data of figure 44 have low strain rate sensitivity at 500 °C, and high sensitivity at 600 °C and 700 °C. Creep is strain rate sensitive at 500 °C, but the creep rates are very small (as seen in figure 43). Since both creep and strain rate sensitivity in tensile testing are becoming notable active between 500 °C and 600 °C, creep could be assisting in a decrease in flow stress with decreasing strain rate. As discussed in Section ??, the barrier for dislocations to move (the yield point), is lowered with increasing temperature. A difference in strain rate, implies a difference in the time a force is applied before the same amount of strain is achieved: for lower strain rates, the time that creep can be active, is larger.

The stress exponent for creep is an indication of the creep rate controlling mechanism. When $n = 1$, diffusion creep occurs by the diffusion of vacancies through the crystal lattice. Sherby and Taleff [39] state that for $n = 2$, dislocation climb is rate controlling (i.e. dislocations move out of their glide

surface). $n = 3$ is the viscous glide of dislocations or can be considered as a transition between diffusion creep and dislocation creep. For $n = 4-6$, dislocation creep is rate controlling through dislocation glide plus climb of lattice diffusions (dislocations move in the surface which contains the dislocation line and its Burgers vector). From the creep data, stress exponents of 2.1 at 500 °C, 5.4 and 5.3 for 600 °C and 700 °C respectively are obtained. Probably both systems are active, whereas dislocation climb is the dominant process between 500 °C - 600 °C, and dislocation glide at 600 °C and 700 °C.

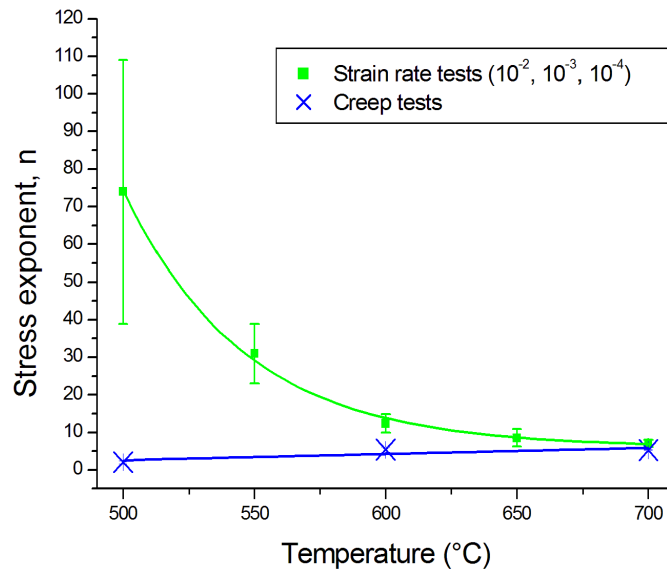


Figure 45: *Stress exponents calculated from creep data and strain rate tests.*

4 Experimental calibration of constitutive equation for creep

In this chapter we will make an effort to construct a model for the prediction of strain or stress relaxation with respect to temperature. We start with the constitutive equation for creep proposed by Sherby and Burke [24]:

$$\dot{\epsilon} = K e^{\frac{-Q_c}{RT}} \sigma^n \quad (22)$$

This equation is extended with the contribution of (changing) grain size and the threshold stress to:

$$\dot{\epsilon} = A \left(\frac{b}{d}\right)^p \left(\frac{\sigma - \sigma_0}{E}\right)^n e^{\frac{-Q_c}{RT}}, \quad (23)$$

with A a material constant, b the magnitude of the Burgers vector, d the grain size diameter, p the grain size exponent, σ the applied stress, σ_0 the threshold stress, E Young's modulus, n the stress exponent, Q_c the activation energy for creep, R the gas constant and T the temperature.

First this equation will be calibrated with creep-data from literature. Second we will tune this equation to the specific properties of our steel of interest with own collected data.

4.1 Calibration with creep-data from literature

AISI 420 in the ferritic phase is not extensively described in literature. However, we found results of a comparable steel in [36] and [37]. The chemical composition of this steel is shown in table 10

C	Cr	Si	Al	Mn	P	S	Mo	Ni	W	Cu	Fe
0.1	18	1	1	0.45	0.024	0.013	0.03	0.30	0.01	0.13	Bal.

Table 10: Chemical composition of comparable steel [37].

The results of the stress relaxation tests are displayed in figure 46

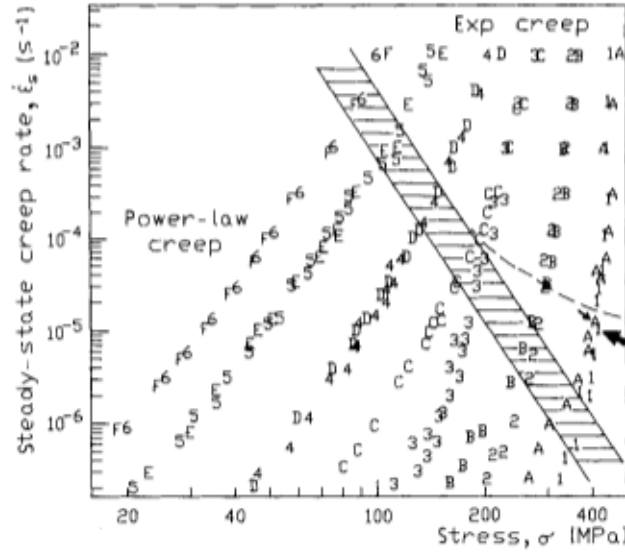


Figure 46: *Steady-state creep properties at: 500 °C (1), 550 °C (2), 600 °C (3), 650 °C (4), 700 °C (5), 750 °C (6). The hatched area marks the transition between power law and exponential creep [36]. The letters A-F represent data of this material, but with coarser grains.*

The strain rate sensitivity m of the flow stress is calculated by taking the slope of a double-logarithmic fit of stress against the strain rate, which has been done in figure 47(a) for three temperatures. Grain growth has not been reported in [37] and $(\frac{b}{d})^p$ can therefore be considered constant. Then, equation 31 in this configuration becomes:

$$\dot{\epsilon} = B + n \ln\left(\frac{\sigma - \sigma_0}{E}\right), \quad (24)$$

where B is a temperature dependent factor. The threshold stress is then determined by plotting the stress against $\dot{\epsilon}^m$ and is the stress at zero strain. For the plotting and calculation of m , values in the power-law regime from figure 47(a) are taken. As shown in figure 47(b) the values of σ_0 are small and independent of the temperature. Since zero and negative values fall within the error bars, we assume the threshold stress to be zero.

The stress exponent n is defined as the inverse of the strain rate sensitivity m and is displayed in figure 48(a). They agree with the values for the power-law creep regime. The values for the other

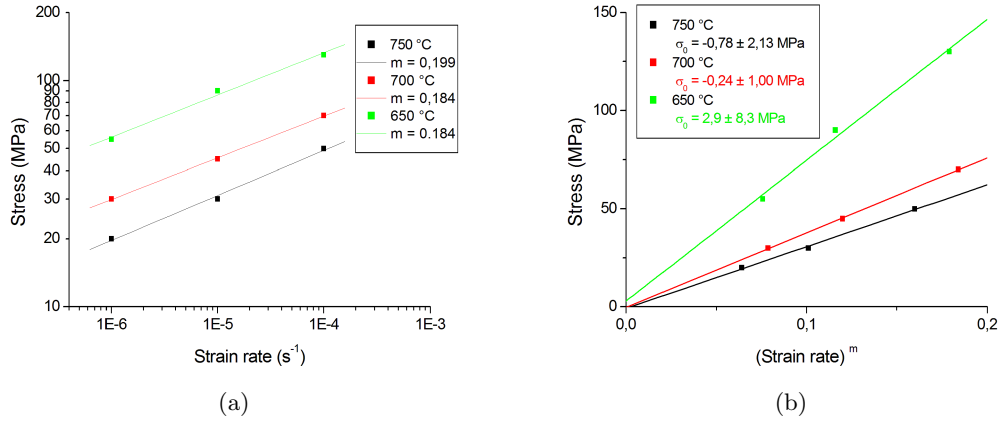


Figure 47: (a) Stress dependence of the strain rate for three temperatures, (b) values of σ_0 for these temperatures from stress against $\dot{\epsilon}^m$, for data taken from figure 46.

temperatures have been taken from this figure and plotted with a linear fit, excluding the point at 600 °C which seems to be an outlier (figure 48(b)). For this temperature and strain rate regime, we therefore consider the stress exponent to be linear dependent on temperature:

$$n = 18.1 - 0.017 * T, \quad (25)$$

with T the temperature in °C.

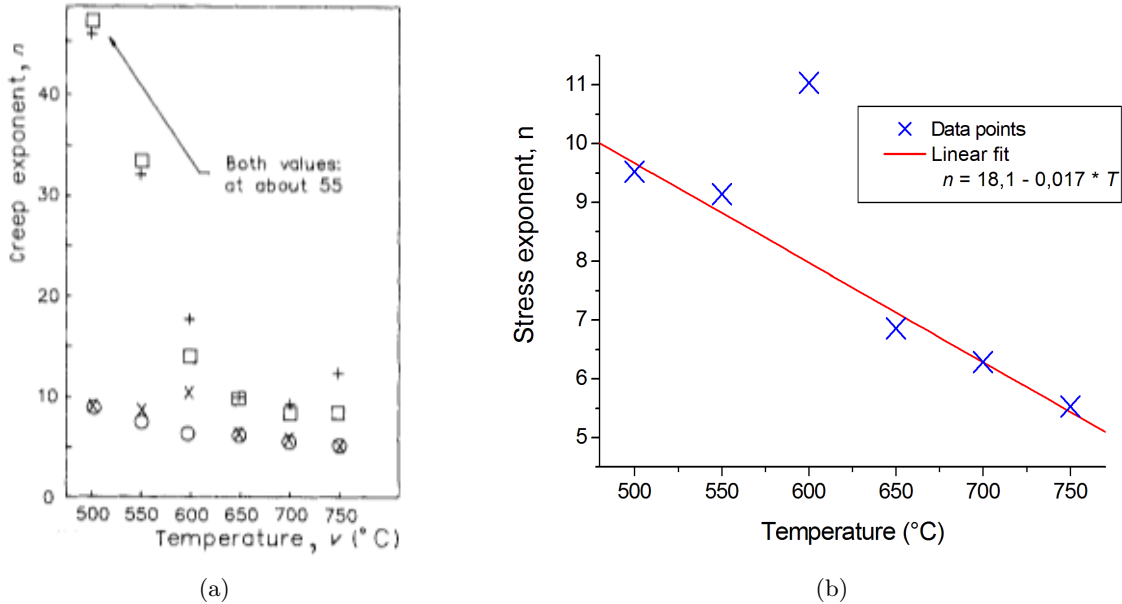


Figure 48: (a) Creep (or stress) exponent n calculated for the power-law region (denoted by x) and the exponential regime (+) [36] and (b) temperature dependence of the stress exponents in this power-law regime.

The activation energy for creep Q_c , as in equation 31, can be estimated from the data of the flow stress

against strain rate in figure 47(a). Barret et al. [20] emphasize that Q_c can be found by plotting $\ln \dot{\epsilon}$ vs. $1/T$ at constant $\frac{\sigma}{E}$, since they state that the apparent Q_c is given by

$$Q_c = \frac{R d \ln \dot{\epsilon}}{d(1/T)} \quad (26)$$

Thus, the vertical separation between the data points at the selected temperatures at constant σ/E , is proportional to the activation energy [40], with E calculated according to equation 16. The results of these calculations are illustrated in figure 49. The smaller strain rate's show a little higher Q_c of 193.9 ± 37.9 kJ/mol with a higher error, compared to 163.6 ± 21.5 kJ/mol and 162.0 ± 23.4 kJ/mol. Barret et al. [20] mention that, according to Sherby [41], the activation energy for volume self diffusion in crystalline metals can be estimated by

$$\frac{Q_{asd}}{T_m} = Rk_0, \quad (27)$$

where R is the gas constant and k_0 a crystal structure factor with value 14 for bcc metals. For our material with $T_m = 1400^\circ\text{C}$, Q_{asd} would be $\approx 195 \text{ kJ/mol}$. Frost and Ashby [38] present values for α -Iron of 251 kJ/mol for lattice diffusion, 175 kJ/mol for boundary and core diffusion.

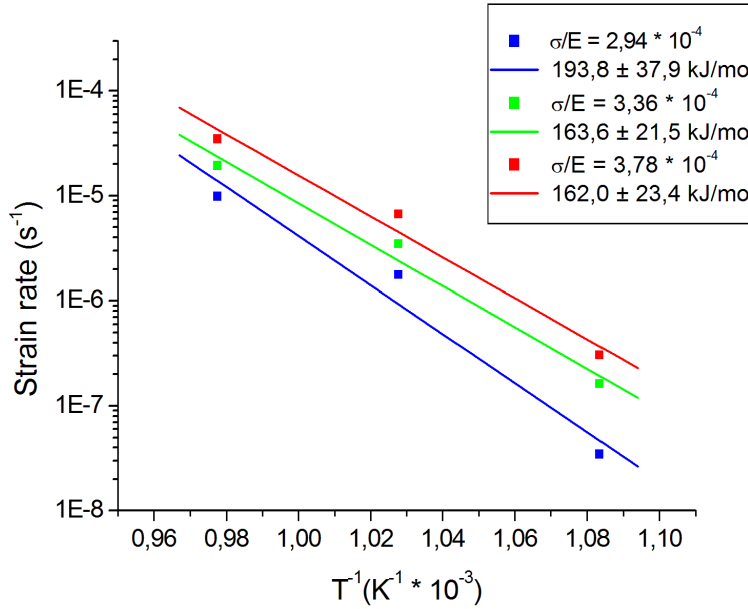


Figure 49: Activation energy for the creep data from figure 46.

4.2 Calibration with experimental creep-data

The method to obtain the constitutive equation for creep, will now be applied to the data obtained by the creep measurements in this work (figure 43). Earlier we concluded that the grains do not change in size during a heat treatment of 30 minutes at 700 °C. Since the creep curves show constant creep rates, we assume that the grains do not grow during the time of measurements.

The strain rate sensitivity m is shown in 50(a), and the threshold stress σ_0 in 50(b). The latter shows values close to zero, which agrees to σ_0 in figure 47(b).

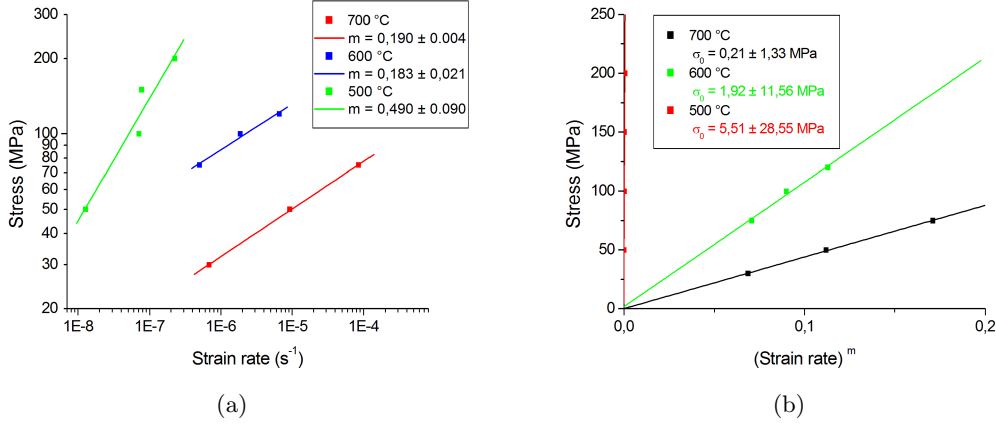


Figure 50: (a) Creep exponent n calculated from the creep data of figure 43 and (b) calculation of the threshold stress.

The determined strain rates at E-modulus compensated stresses at different temperatures, are shown in figure 51. The relation log-strain rate vs. inverse temperature is not linear, i.e. the activation energy is not constant in this temperature range. Therefore we calculated the activation energy in two parts: one from the fit between 500 °C and 600 °C, and between 600 °C and 700 °C, as indicated in figure 51 by dotted lines. The values are listed in table 11

σ/E	Q_c : 500 °C-600 °C (kJ/mol)	Q_c : 600 °C-700 °C (kJ/mol)
$7,96 * 10^{-4}$	87	139
$5,57 * 10^{-4}$	57	141
$32,6 * 10^{-4}$	28	143
average	57,3	141

Table 11: Activation energies calculated from two points.

These activation energies are lower than the Q_c for lattice diffusion of α -Iron (as shown in section 4.1). However, Da Silva [27] reports an activation energy for the diffusion of carbon in α -Iron of 78 kJ/mol. Between 500 °C and 600 °C, the activation energy for creep becomes higher than 78 kJ/mol, for a load higher than $\frac{\sigma}{E} = 7.96 * 10^{-4}$ (table 11), which corresponds to a stress of about 110 MPa. In figure 43 can be seen that the creep rate at 500 °C becomes three times higher for a load of 200 MPa, compared to 150 MPa. This suggest that the diffusion of carbon plays an important role in the creep behavior of this steel.

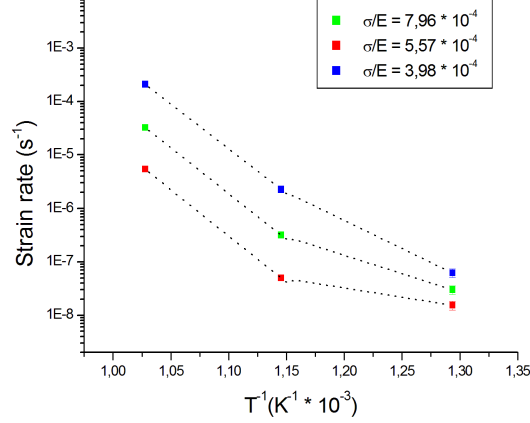


Figure 51: Variation of the strain rate as a function of the inverse temperature for E -modulus compensated stresses.

The material constant A is calculated by taking the known stress and strain rate, the calculated stress exponent and the estimated activation energy and balance the constitutive equation. The result is the proposed equation with an interpolation between 500°C and 600°C for the material constant, stress exponent and activation energy. Between 600°C and 700°C the material constant is interpolated and the (small) change in the stress exponent is taken into account. The result is a constitutive equation of the form

$$\dot{\epsilon} = A(T) \left(\frac{\sigma}{E(T)} \right)^{n(T)} e^{\frac{-Q_c(T)}{RT}}, \quad (28)$$

with values of:

$$\dot{\epsilon} = (-123 + 0.16 * T) \left(\frac{\sigma}{E(T)} \right)^{-23+0.033*T} e^{\frac{(-589+0.084*T)*1000}{RT}}, \text{ for } T \text{ between } 773 \text{ and } 873^{\circ}\text{K} \quad (29)$$

$$\dot{\epsilon} = (-12 + 0.008 * T) \left(\frac{\sigma}{E(T)} \right)^{-6.6-0.001*T} e^{\frac{(-141)*1000}{RT}}, \text{ for } T \text{ between } 873 \text{ and } 973^{\circ}\text{K}. \quad (30)$$

5 Finite Element Method implementation

In physics and engineering, simulation is a powerful tool to reveal the influence of model parameters and calculate the behavior of a new product design. A common and wide spread use is a Finite Element Method (FEM) calculation. A FEM is a robust method to model numerically the behavior of a material with application of stress, strain and temperature. Goal is to calculate the displacements and stresses everywhere in a deforming body. The development of powerful computers in the past decades allows FEM solvers to calculate more complex problems with increasing detail and parameters.

A general description of a FEM is given in [42]. In the FEM, the body of interest is divided into a set of intervals named finite elements. The lines come together at intersection called nodes. Each element has as least four integration points where calculations are performed. These values are extrapolated towards the nodes, where an average is taken. The average yields then as the value of the elements at that node. The collection of the lines and nodes are the finite element mesh of the body (see figure 52). This approach has two reasons: a body can consist of different parts, where the solutions of this finite elements are represented by different functions. Second, the solution over a finite number of elements is simpler to calculate then an approximation over the whole domain.

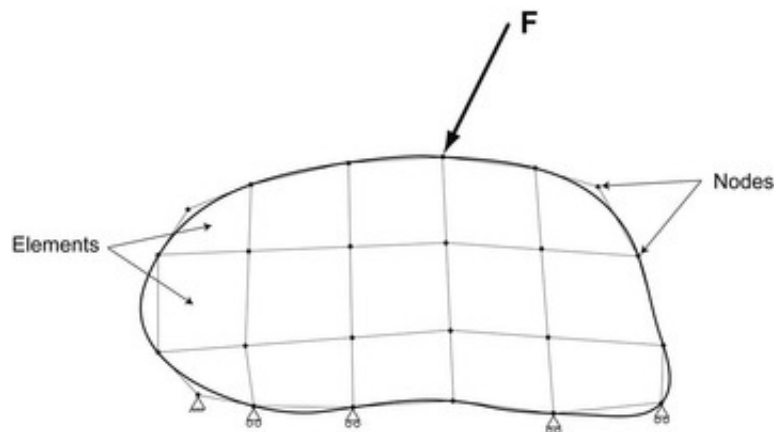


Figure 52: *Illustration of a finite element body indicating the nodes and line elements which form the mesh [43].*

The FEM software that has been used is Cyrstal, a solver developed by Philips. The structure of this FEM package is illustrated in figure 53 and shows its three parts: the pre-processor, the solver and the post-processor. The pre-processor creates the files which define the model. This includes the definitions and geometries of the tools used in the simulation and the mesh. The solver, Crystal, uses the files from the pre-processor with the *.inp file as the the main input. The *.iss file contains the initial values for eacht integration point, while the mesh is defined in the *.msh file. The material model is stored in lookup tables which are governed in the *.mmf file. The lookup tables contain the values of state variables like the Equivalent plastic strain, Von Mises stress, Dislocation density, Flowstress and E-modulus. The advantage of the lookup tables is the flexibility for implementing new models, like the calibrated creep model, without the need of re-programming the solver. After the calculations of the solver, the post-processor interprets the results and creates an output. A typically input file can be found in Appendix B. Further detailed information about the FEM with Crystal can be found

in [44], where the above structure and a complete implementation of a new material model in Crystal are described.

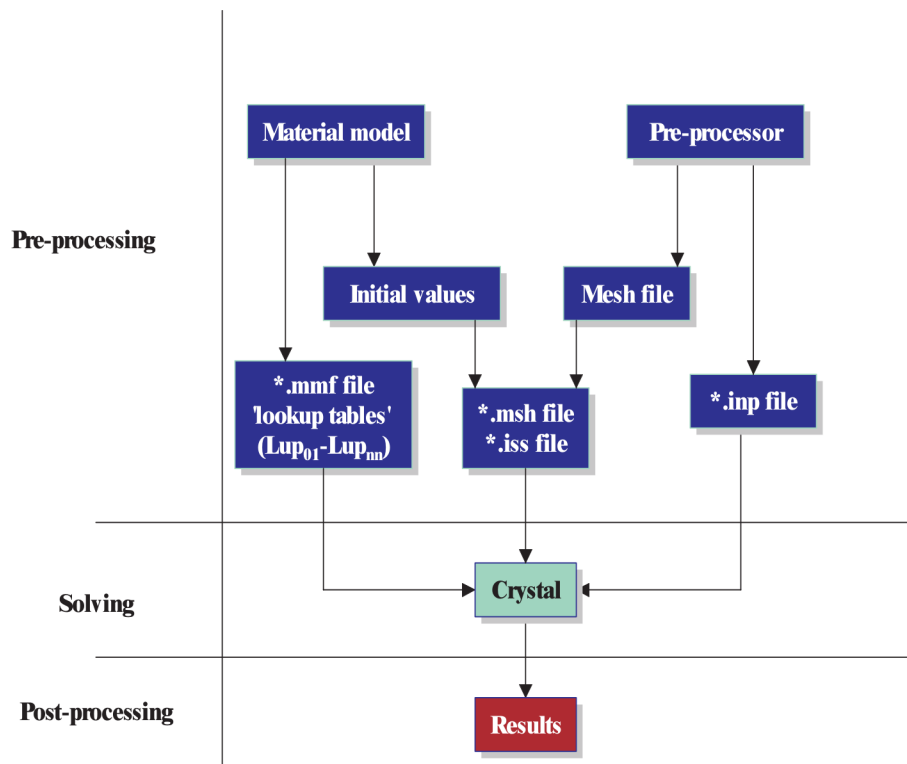


Figure 53: *File structure of the Crystal FEM solver [44].*

The calibrated creep model has been implemented into Crystal in means of a new material model with the temperature dependent E-modulus as derived in this work. The creation of the lookup tables has been done with Matlab [9], a selection of the code can be found in Appendix C. The temperature and stress tables consist of 150 elements of equal length in the range 273 - 1023 °K and 0 - 400 MPa respectively.

Validation by comparing FEM calculation with creep test results

The precision after implementation of this model is validated by the calculation of a single element creep test at 700 °C with a load of 50 MPa. A constant virtual tension of 50 MPa is applied, where after the element is heated to 700 °C in 2 seconds and kept constant afterwards. This simulation is shown in figure 54. The creep strain diagram on the right side has two plots: the creep strain of the model in red and the (FEM) one element calculation in blue. The strain of the model is calculated by direct integration of the strain rate values of the lookup tables with respect to the stress level and temperature. The strain of the FEM calculation is a step by step integration of the element where the stress, temperature and contribution of other elements are evaluated at every time step. Since one element at a constant temperature and stress below the yield point is considered, the values are expected to be similar. By applying a linear fit through the data, the strain rate is obtained. The model gives 9.75×10^{-6} , FEM 9.98×10^{-6} , whilst the (real) creep test (figure 43) gives 9.26×10^{-6} . The difference between the (real) creep test and the model simulation is due to the fitting of the creep model parameters. The small difference between the model and the FEM calculations is due to rounding off errors in the FEM, since this is a step by step evaluation at every integration point where small fluctuations in the precision could lead to a minor addition in the creep strain.

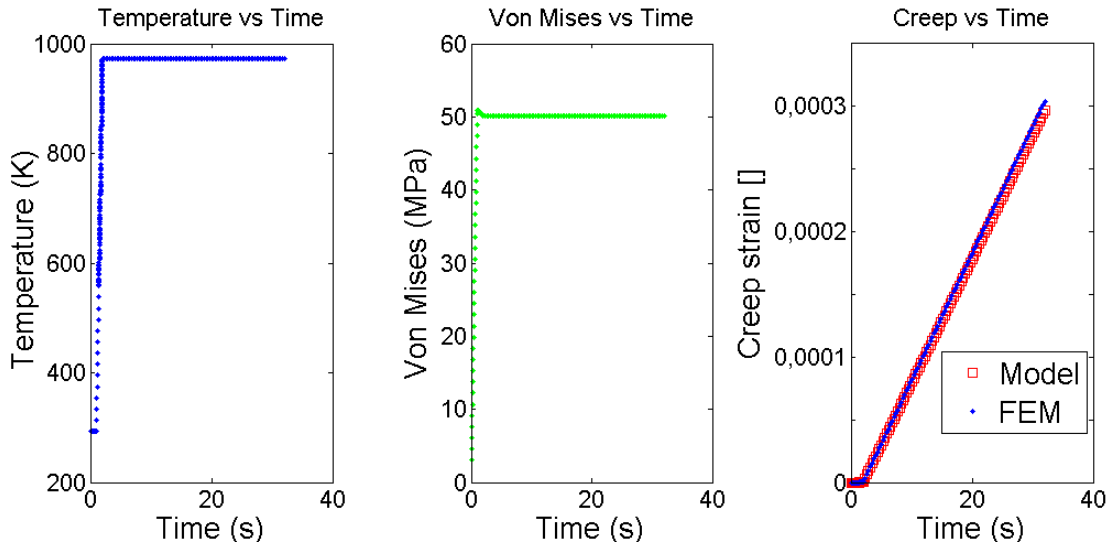


Figure 54: *Diagrams of temperature, stress and creep strain vs. time of a simulated creep test.*

Validation by comparing FEM calculation with stress relaxation test results

The second validation of the model is a calculation of a stress relaxation test with 15 elements. A sample of 5 by 3 elements is heated to 700 °C, bended between two tilted dies until a stress of 50 MPa is reached in the top element. After that, the dies are fixed in their final position and the temperature maintained at 700 °C. From the stress-time plot in figure 55, it is clear that the stress relaxes with time at constant temperature. The strain rate decreases as the stress relaxes. This corresponds to the conclusions drawn from the creep test at constant temperature (figure 43): a lower (or decreasing) load corresponds to smaller strain rates. The creep strain calculated from the model and the FEM agree also for this test, confirming the accuracy of the implementation.

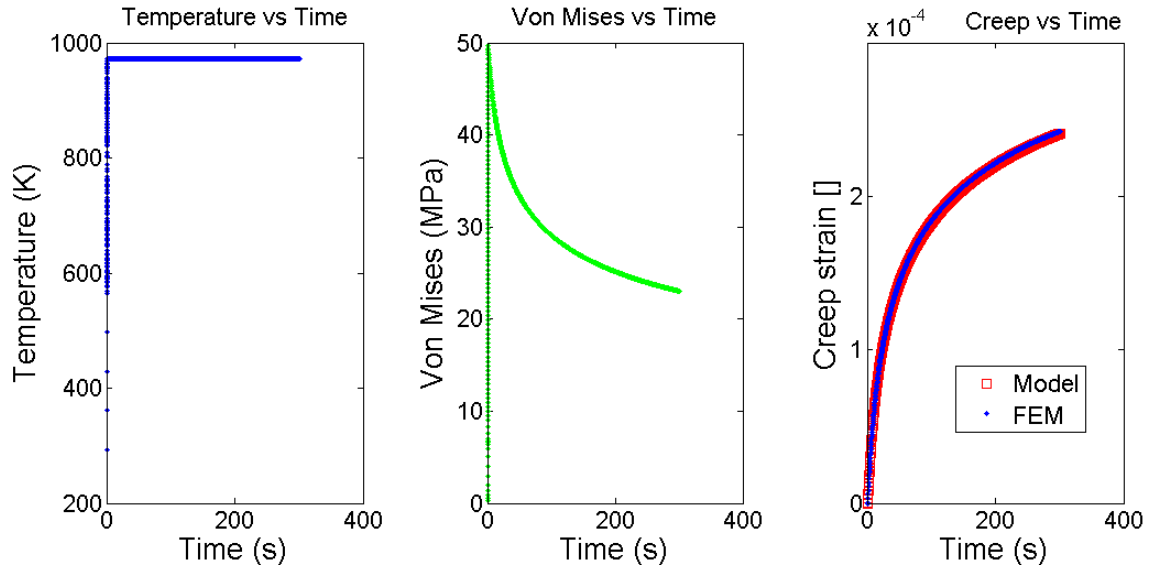


Figure 55: *Diagrams of temperature, stress and creep strain vs. time of a simulated stress relaxation test.*

The calculation as described above has been done for different loads below the yield point at three temperatures. The results have been compared to (real) stress relaxation tests in figure 56. All results show the same behavior: at the same temperature, stress relaxes more when the load is higher and the stress relaxation is stronger at higher temperature. E.g. the sample at 500 °C relaxes from 160 to 138 MPa, at 600 °C from 160 to 90 MPa after 100 seconds. The model however shows little relaxation at 500 °C and goes from 160 to 159 MPa, but relaxes comparable to the test at 600 °C by going from 160 to 94 MPa. There could be an anelastic (or viscoelastic) effect in the stress relaxation, which the model does not take into account.

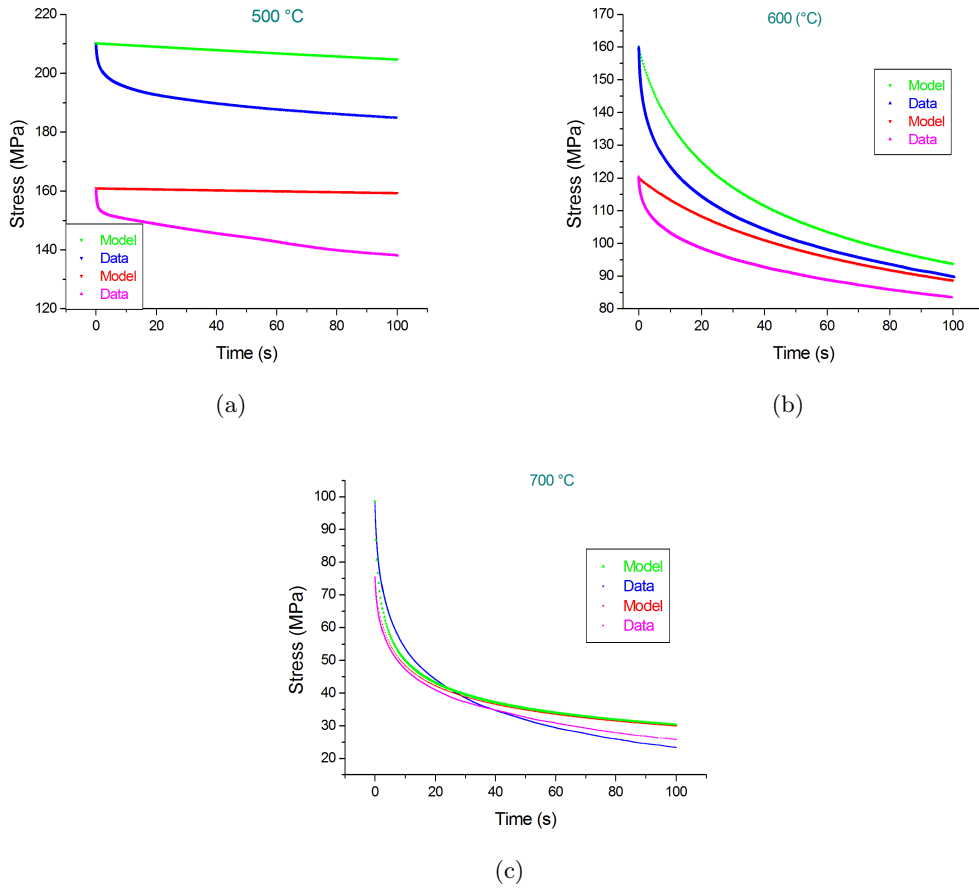


Figure 56: Simulated model stress relaxation compared to real tests (denoted as data) for: (a) 500 °C, (b) 600 °C and (c) 700 °C.

An illustration of the stress distribution in the sample during a stress relaxation simulation has been made with MSC Marc [45] software and is shown in figure 57. The sample has been divided into a grid of 1 x 10 elements to elucidate the stress distribution. The horizontal line in the center is the neutral axis, where the stresses are zero. The rotational point of the dies is below each illustration. Therefore, the stresses above the neutral axis are tensile, and below the axis compressive. At the start of the simulation, the stress in the top and bottom elements is 50 MPa. Over time, the stresses decrease (or relax) where the elements with stresses of 50 MPa relax faster than the other elements (with exception of the neutral axis where the stresses are zero from the start).

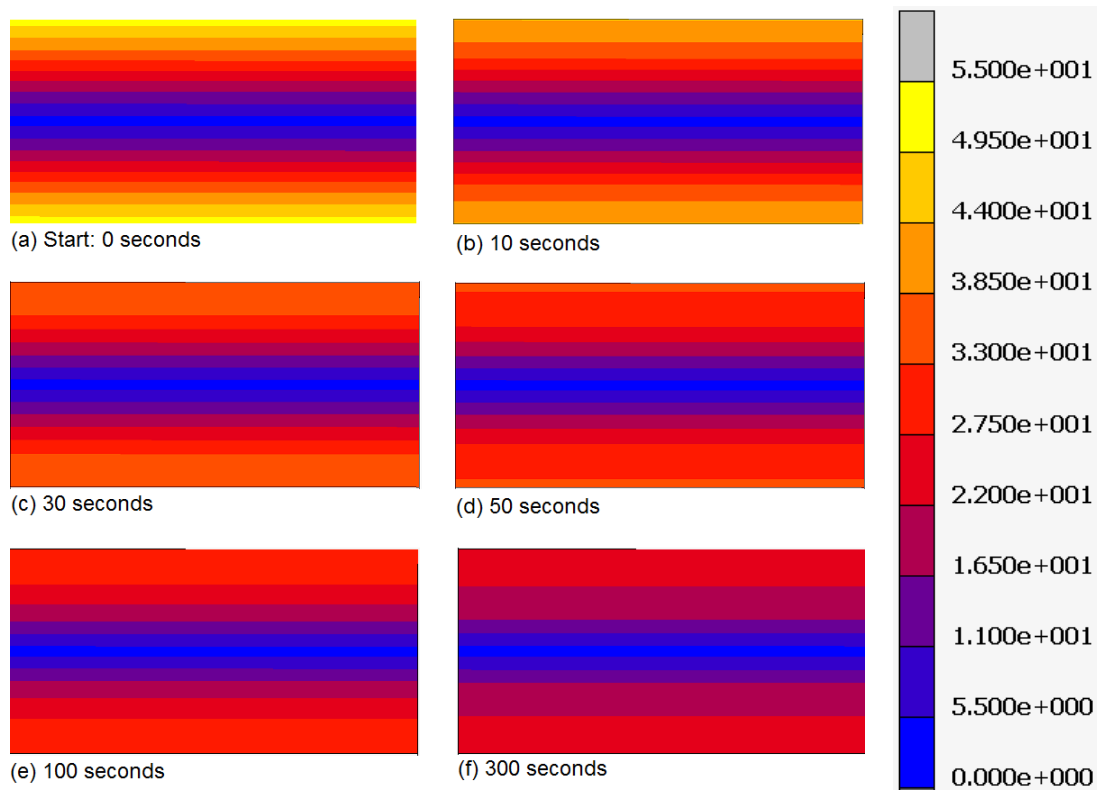


Figure 57: *Simulated stress relaxation of a bended sample.*

Applying creep model on deep drawn section with heat treatment

A three-dimensional calculation on a deep drawn cup with a flat top (figure 58(a)) has been done to demonstrate the influence of the creep behavior during a heat treatment. The deep drawing test is axi-symmetric, therefore a quarter of the cup (figure 58(b)) has been simulated to reduce the number of elements. A two-dimensional simulation of the one-stage deep drawing is shown in figure 59. At the start (a), the segment lies between two dies. When the left die moves downwards, (b) - (e), the stress in all elements increases. Particularly the horizontal and the right side of the sample exceed the yield point of 360 MPa, and the grey parts are stresses above the limit of the scale (> 700 MPa). The deep drawing and the plastic deformation stops after 0.10 seconds (figure 59(e)). The final shape after forming and the stress distribution is shown in figure 59(f).



Figure 58: *a) whole and b) quarter of the cup after deep drawing.*

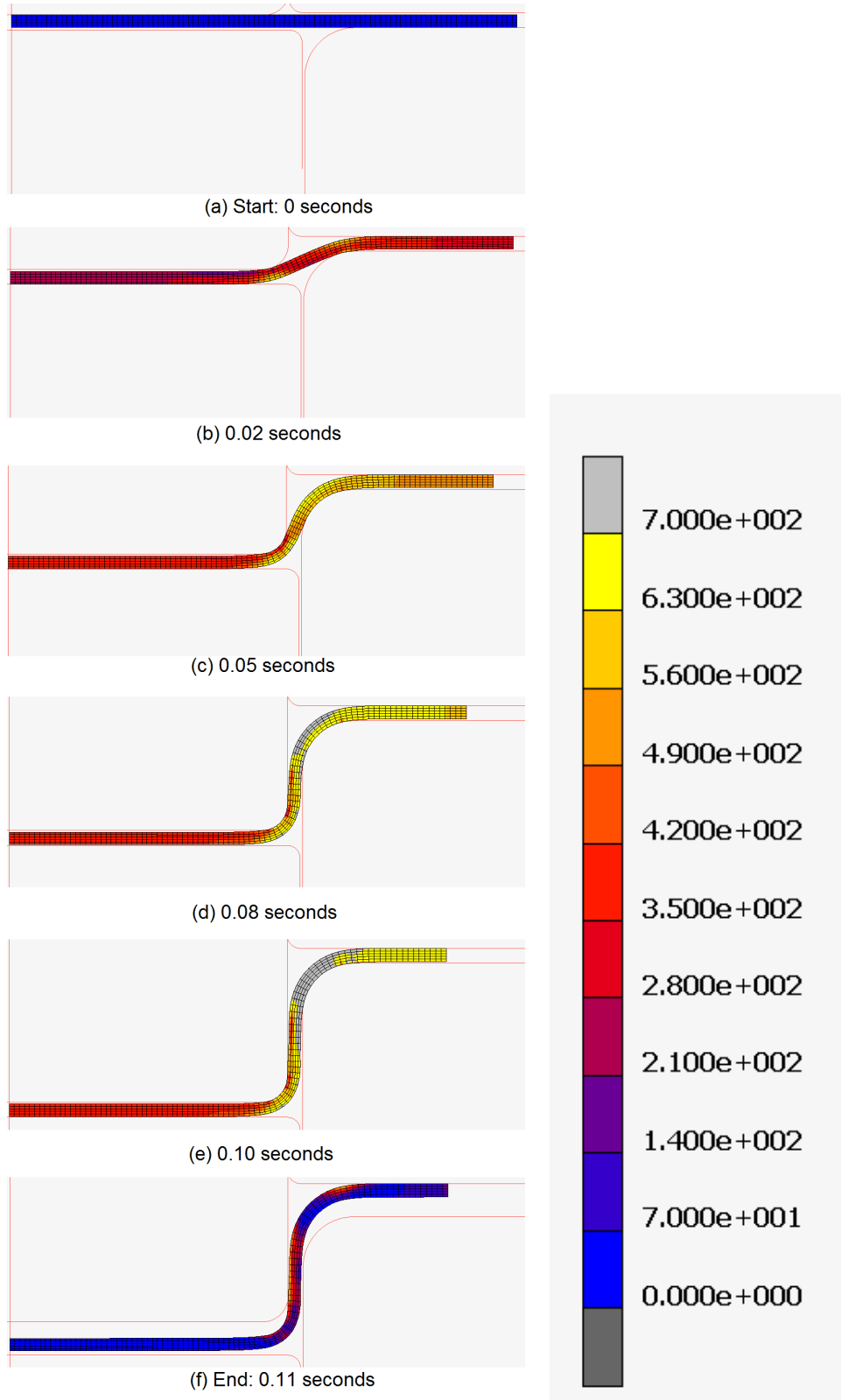


Figure 59: *Two-dimensional simulation of forming a cup with one-stage deep drawing and the distribution of the Von Mises stress.*

This formed section is then heated with $10^\circ/s$ to 500°C . The creep rate in this temperature range is of magnitude below $10^{-7}/s$ (as concluded from figure 43) and the creep, with respect of the time, neglected. The rate of $10^\circ/s$ is similar to the heating rate the caps experience in the belt furnace. The cup is then heated from 500°C to 700°C with $20^\circ/s$. This rate has been chosen to show that in the short time of 10 seconds, the majority of the stresses relax. The sample is then held at 700°C for 10 seconds and cooled down to room temperature with $10^\circ/s$, as shown in figure 60

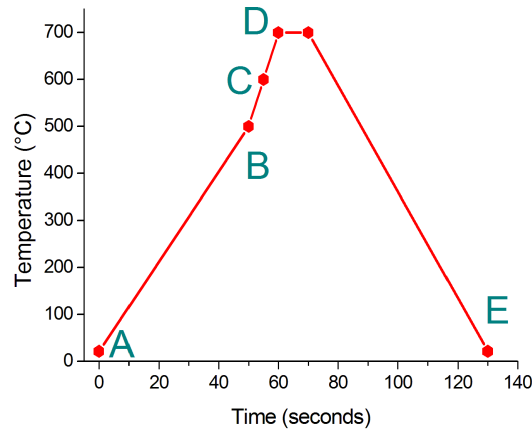
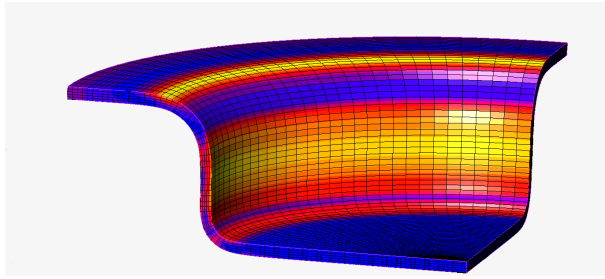


Figure 60: *Temperature profile of the heat treatment which the simulated deep drawn cup undergoes.*

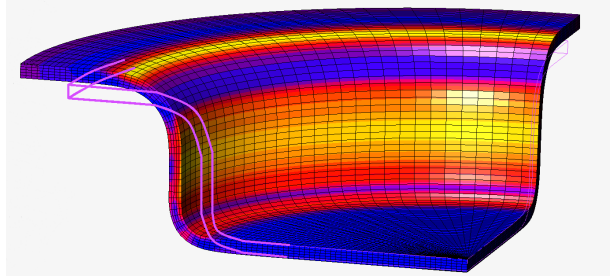
The three-dimensional simulation of the heat treated cup is shown in figure 61, where the indices (a)-(e) correspond to the points A-E in figure 60:

- (a) Initial shape and stress distribution after forming as the result of the one-stage deep drawing in figure 59
- (b) The cup is heated to 500°C . The initial shape is denoted by the pink lines and are highlighted at the left part of the cup. The cap has grown due to thermal expansion (for illustration purposes the shape changes are increased 20 times). The stresses are similar as in (a), since no stress relaxation was allowed below 500°C .
- (c) The cup is at 600°C . The creep model is applied and stresses start to relax. A decrease from 700 to about 490 MPa is observed in the high stress areas .
- (d) Top temperature of 700°C is reached. All elements have been relaxed to stresses below 70 MPa.
- (e) After 10 seconds at 700°C , the cup is cooled down to room temperature. In the left upper corner can be seen that the cup has a different shape than before the heating cycle (initial shape highlighted in pink).

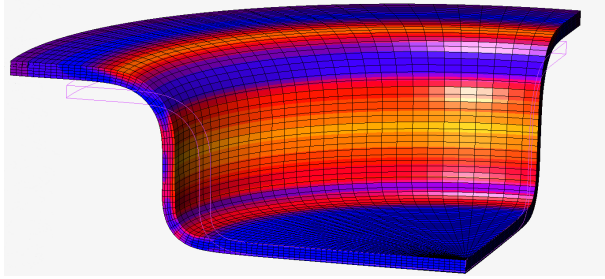
The upper side finally is irreversible changed to a position which is, at the end of the cup, $2/3$ of the thickness lower. Since the cup is 0.5 mm thick and the shape changes where magnified 20 times, the distortion corresponds to a length of $17\ \mu\text{m}$, which is in the order of the distortion shaver caps have.



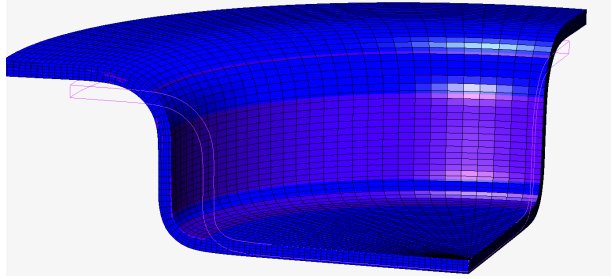
(a) Start at 0 seconds: room temperature



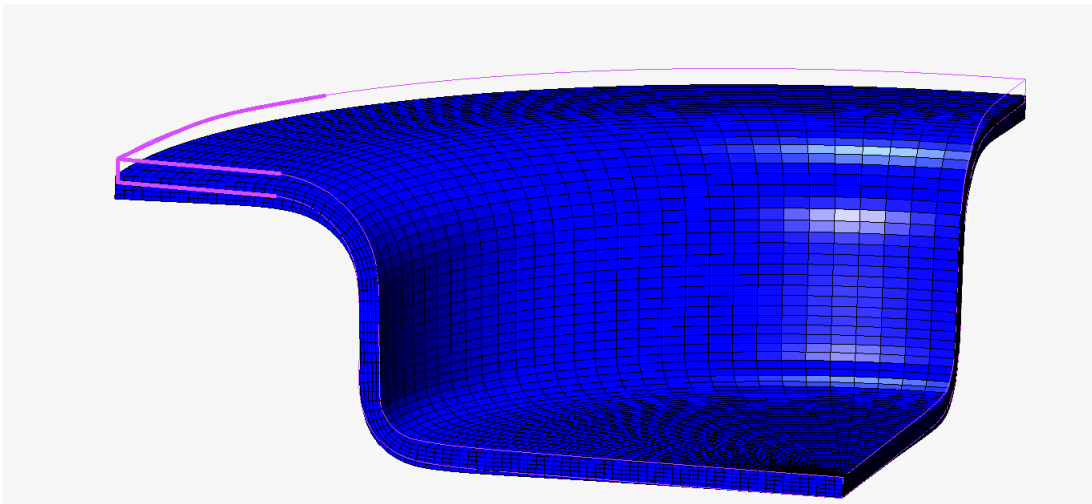
(b) 50 seconds: 500 °C



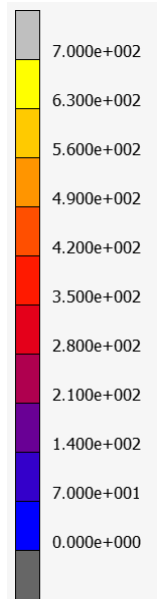
(c) 55 seconds: 600 °C



(d) 60 seconds: 700 °C



(e) 130 seconds: cooled down to room temperature



(f) legenda

Figure 61: 3D simulation of heat treatment of a deep drawn section of a cup. Shape changes are increased 20 times.

6 Conclusions and outlook

The aim of this study was to optimize a model that can predict the shape change of the caps during the heat treatment. Therefore the different processes and properties of the material that are active during hardening have been investigated.

Microstructure

The material is an AISI 420 type of stainless steel which is fully ferritic in the as received condition. It has a clear texture in the rolling direction, even after a heat treatment of 30 minutes at 700 °C, indicating that the material can exhibit anisotropic behavior. The grain size does not change significantly with this heat treatment, but the internal structure does. With misorientation plots it is shown that the material in the as received condition, contains strain in the grains. The misorientations group around the present carbides with a size of about 1 μm . The initial strains in the grains disappear after annealing for 5 minutes at 500 °C.

Transformation characteristics

With dilatometry it is shown that austenization starts at 809 °C. Anisotropy does not have an influence on the (constant) reversible part and the austenization temperature. It seems that above 400 °C, samples perpendicular to the rolling direction have an irreversible positive increase in length, compared to samples parallel to the rolling direction. The length change at the starting point of austenization is for the perpendicular samples slightly higher. If the material in the austenite phase is cooled with a rate higher than 50 °C/min, no perlite is formed and martensite starts to form at 360 °C.

Mechanical properties

The 0.5 mm thick material has an E-modulus of 204 ± 4 GPa in the rolling direction and higher values of 224 ± 2 in the transversal and 227 ± 1 GPa in the 45° direction. The E-modulus at elevated temperatures has been determined with tensile tests. From these data, a linear decrease of the E-modulus with increasing temperature has been derived. Due to the change in behavior of the material at elevated temperature, the E-modulus is difficult to determine with a tensile test, resulting in a lot of spread in the data. Therefore, the proposed linear fit could possibly not be the true relation.

Modeling creep behavior

A creep model has been calibrated with the experimental data of the tests in this work. From creep data, stress exponents of 2.1 at 500 °C, dislocation climb, 5.4 and 5.3 for 600 °C and 700 °C respectively are obtained. Probably two main systems are active for creep, whereas dislocation climb is the dominant process between 500 °C - 600 °C, and dislocation glide at 600 °C and 700 °C. Due to this change in dominant process, the stress exponent, activation energy and material constant of the basic equation

$$\dot{\epsilon} = A \left(\frac{b}{d}\right)^p \left(\frac{\sigma - \sigma_0}{E}\right)^n e^{-\frac{Q_c}{RT}}, \quad (31)$$

have been made temperature dependent:

$$\dot{\epsilon} = A(T) \left(\frac{\sigma}{E(T)}\right)^{n(T)} e^{-\frac{Q_c(T)}{RT}}, \quad (32)$$

The calibrated creep model is implemented in a finite element solver, and validated by comparing the calculations to creep and stress relaxation tests. The calculations of creep agree very well with the experiments. Simulation of stress relaxation yields the same result as tests conducted at 700 °C,

but shows a discrepancy at 500 °C, probably due to anelastic effects which have not been taken into account. It is also shown that for a cup, creep causes irreversible shape changes for temperatures below the austenization point. These distortions of the cup are in the order of the final distortions shaver caps have after they have undergone a full hardening cycle.

Outlook

Modeling

Future research can make the model more robust. Bulk properties are not sufficient parameters when modeling is done on this precise scale. Dilatometry, with the developed technique to analyze thin samples without constraints, is a very powerful application to characterize the properties of the samples on this scale. The anisotropic effect on the heating trajectory can be quantified more with additional repetitions of the performed measurements, but also in the 45 ° direction and on samples of this material, with different thicknesses. Validation, calibration and a better understanding of the model could be obtained by performing dilatometer tests on pre-strained samples or stresses induced by applying a load during the test. Dynamic E-modulus dependence on temperature could also be done with this technique. Also viscoelastic behavior can be studied by applying a sinusoidal force and determine the storage and loss modulus. Young's modulus at elevated temperature could also be measured with an ultrasonic pulse-sing around method, as described in [46].

The next step for improving the model is to make it directional-dependent by including the anisotropic effects and expanding the model to the austenite regime. Therefore, creep tests as performed in this work need to be done and a precise model for the E-modulus as a function of temperature is needed. The anelastic behavior, which is visible in the stress relaxation tests, should be investigated more and taken into account to predict the stress relaxation more precise.

Production

Without considering the tool which is used by forming, some ideas could improve the shaver caps as well. First by annealing the strip material before the forming step. The small amount of strain it contains will be relieved and the flow stress will be lower. Five minutes at 300 °C - 500 °C will be sufficient to, at least, relieve the strain. At higher temperatures (700 °C) the drop in the yield point will disappear. The material will become more homogeneous and behave more predictable and equal in all directions.

After forming, the shaver caps contain residual stresses. When the caps are put into the furnace for hardening, the stresses relief (due to increase in temperature) and simultaneous creep increases (due to increase in temperature). Notable stress relief is activated between 500 °C and 600 °C; notable creep rates appear at temperatures between 600 °C and 700 °C. In all cases, creep rates are higher for higher initial stresses. With this in mind, we recommend to investigate the possibility of keeping the shaver caps for a longer time at 500 °C - 600 °C, to relief stresses but limit the amount of creep. In addition, the deep drawing should be performed in the way that the influence of creep and stress relaxation on the shape of the shaver cap, is minimized

7 Acknowledgments

Lectori salutem!

This chapter is the last part of my thesis, thank you for reading all of the above! These last words do not only mark the final part of my thesis, but also the end of an inspiring time. I had a great year in which I had the opportunity to increase my knowledge in physics, mastering measuring techniques, and to work with and learn from highly skilled professionals. Discussing each others results and collaboration has been very important to improve my research and resolve problems.

I want to thank Professor De Hosson for providing me a place in his group. You helped me by taking the time to explore and discuss research topics. I'm very happy with your help to do my research within Philips and the MK-group. I also want to thank you for your overview on the topic and stimulating me to -apologies for the translation- "find the meatballs in the scientific soup".

Special thanks to Dr. Václav Ocelík: as my daily supervisor in the MK-group you have taught me a lot on physics in general, and specific on electron microscopy. Thank you for always finding some space in your agenda to answer my (many) questions!

I would also thank Manso Groen. Thank you, not only for supervising my work within Philips, but also for your collaboration. You introduced me into the different fields one has to master to perform model- and product simulations. It was fun and inspiring to work with you!

For the modeling and general interest, I want to thank Gerrit Klaseboer. You provided a lot of support and feedback, it was very helpful for me to try to answer your questions!

Ronald, thank you for learning me to handle the tensile bench and your efforts to optimize our high temperature tests! I would also thank you for emphasizing that one has to control first the well known (physical) parameters and then try to optimize with the help of electronics and software.

Henkjan, thanks for making the technical drawings and your help with the bending tests!

Thanks to all of the people of Philips Drachten, especially within the Process Engineering group and "the office" of the ground floor in the ATC. You really made me feel as one of your colleagues and provided me the opportunity to improve my game of table football!

This also yields for my fellow students and researchers of the MK-group. Thank you for showing interest in my topic, especially Leo for your collaboration!

Last-but-one, I want to thank my parents and my family for their support!

The last person I want to thank, is the first in my life: my fiancée Dieudonné! Thank you for your love and being in my life! I deeply appreciate your support and that you always made time to listen to my stories about my research, tensile testing, dislocations, electrical shavers, creep, ... **You're fantastic!!!**

References

- [1] <http://www.smt.sandvik.com/en/materials-center/material-datasheets/strip-steel/sandvik-6c27/>
- [2] ASM Speciality Handbook - Stainless Steels, ISBN 0-87170-503-6 (1994), p.13
- [3] R.O. Duda, P.E. Hart, "Use of hough transform to detect lines and curves in picture" Communications of the ACM, 15(1), 11-15 (1972).
- [4] http://www.doitpoms.ac.uk/tlplib/crystallographic_texture/texture_representation.php
- [5] <http://fiedler-oe.com/en/products/lex/parallel.html>
- [6] <http://fiedler-oe.com/en/products/lex/hightemp.html>
- [7] M. Hommes, "Evaluation report laser extension meter", Internal report Phillips (2001)
- [8] G.E. Dieter, "Mechanical Metallurgy", ISBN 0-07-100406-8 (1961), p.139
- [9] MATLAB and Statistics Toolbox Release 2010b, The MathWorks, Inc., Natick, Massachusetts, United States
- [10] <http://www.tainstruments.com/product.aspx?siteid=11&id=198&n=1>
- [11] D.M. Price, "Modulated-temperature thermomechanical analysis", Thermochemica Acta 357-358 (2000) 23-29
- [12] W.D. Callister, "Materials Science and Engineering an Introduction", Wiley, 7th edition (2007), p.290-291
- [13] ScottV, <http://people.tribe.net/scottthesculptor/photos/53c3eae8-d1d1-44a9-83d4-12269c50676f>
- [14] M. Gajewska et al., "Instability of plastic flow and their role in texture transformations", presentation
- [15] L.N. Brewer, M.A. Othon, L.M. Young, T.M. Angeliu, "Misorientation Mapping for Visualization of Plastic Deformation via Electron Back-Scattered Diffraction", Microsc. Microanal. 12 (2006) 85-91
- [16] M.Kamaya, "Characterization of microstructural damage due to low-cycle fatigue by EBSD observation", Materials Characterization, 60 (2009) 1454-1462
- [17] M.Kamaya, "Assessment of local deformation using EBSD: Quantification of accuracy of measurement and definition of local gradient", Ultramicroscopy, 111 (2011) 1189-1199
- [18] M.Kamaya, "Assessment of local deformation using EBSD: Quantification of local damage at grain boundaries", Materials Characterization, 66 (2012) 56-67
- [19] TSL OIM software from EDAX, <http://www.edax.com>
- [20] C.R. Barrett, A.J. Ardell, O.D. Sherby, "Influence of modulus on temperature dependence of activation energy for creep at high temperatures", Transactions of the metallurgical society of Aime, Vol.230, 1 (1964) p.200

- [21] ASM Speciality Handbook - Stainless Steels, ISBN 0-87170-503-6 (1994), p.10
- [22] University of Cambridge, <http://www.doitpoms.ac.uk/tlplib/creep/printall.php>
- [23] Oxford Instruments, <http://www.ebsd.com>
- [24] O.D. Sherby, P.M. Burke, "*Mechanical Behavior of Crystalline Solids at Elevated Temperature*", Prog Mater Sci 13:323 (1968)
- [25] P. Guyot, E. Ruedl, "*Deformation Mechanisms of Metals Hardened by a Dispersed, Incoherent, Second Phase*", J. Materials Science, 2 (1967) 221
- [26] M.M. Hall, "*Thermally Activated Dislocation Creep Model for Primary Water Stress Corrosion Cracking of NiCrFe Alloys*", Presented at the International Symposium on Plant Aging and Life Prediction of Corrodible Structures, Japan Society of Corrosion Engineering, Sapporo, Japan, No. WAPD-T-3045; CONF-9505335-1 (1995)
- [27] J.R.G. da Silva, R.B. McLellan, "*Diffusion of Carbon and Nitrogen in B.C.C. Iron*", Materials Science and Engineering, 26 (1976) 83-87
- [28] J. Cheng, B. Young, B. Uy, "*Behavior of high strength structural steel at elevated temperatures*", Journal of Structural Engineering, 132(12) (2006) 1948-1954
- [29] M. Fukuhara, A. Sanpei, "*Elastic moduli and internal friction of low carbon and stainless steels as a function of temperature*", ISIJ International, Vol. 33 (1993) No. 4, 508-512
- [30] W.H. Hill, K.D. Shimmin, "*Elevated temperature dynamic elastic moduli of various metallic materials*", Wright-Patterson Air Force Base, Ohio, Wright Air Development Division Air Research and Development Command, U. S. Air Force (1961)
- [31] H.Masumote, S. Sawaya, M. Kikuchi, "*Thermal Expansion and Temperature Dependence of Young's Modulus in Fe-Cr Alloys*", Transactions of Japan Institute of Metals, Vol.12 (1971) No. 2, 86-89
- [32] R. E. Smallman, R. J. Bishop, "*Metals and materials: science, processes and applications*", ISBN 978-0-7506-1093-3 (1995), p. 206
- [33] A. H. Cottrell, B. A. Bilby, "*Dislocation Theory of Yielding and Strain Ageing of Iron*" (1949), Proc. Phys. Soc. A 62 49
- [34] D. Hull, D.J. Bacon, "*Introduction to dislocations*", Elsevier, Fifth ed. (2011)
- [35] A.Rose et al., "*Atlas zur Wärmbehandlung der Stähle*", Verlag Stahleisen, Düsseldorf, 1958
- [36] F. Groisbck, "*Creep behaviour of a heat-resistant ferritic chromium steel in terms of stress exponents*", J. Materials Science, 27 (1992) 4373-4380
- [37] F. Groisbck, F. Jeglitsch, "*Internal and effective stresses in high-temperature creep evaluated from transient dip tests and dislocation bowing*", J. Materials Science, 27 (1992) 4365-4372
- [38] H.J. Frost, M.F. Ashby, "*Deformation-Mechanism Maps, The Plasticity and Creep of Metals and Ceramics*", web version, <http://engineering.dartmouth.edu/defmech/>

- [39] O.D. Sherby, E.M. Taleff, "*Influence of grains size, solute atoms and second-phase particles on creep behavior of polycrystalline solids*", Materials Science and Engineering A322 (2002) p. 89-99
- [40] A.V. Kazantzis, Z.G. Chen, J.Th.M. De Hosson, "*Deformation mechanism of aluminium-magnesium alloys at elevated temperatures*", J. Mater. Sci., 48 21 p.7399-7408 (2013)
- [41] O.D. Sherby, M.T. Simnad, "*Prediction of Atomic Mobility in Metallic Systems*", Transactions ASM 54 (1961) 227
- [42] J.N. Reddy, "*An introduction to the Finite Element Method*" (Third ed.), McGraw-Hill, ISBN 9780071267618 (2005)
- [43] E.F. Morgan, M.L. Bouxsein, "*Use of finite element analysis to assess bone strength*", BoneKEY-Osteovision 2 (2005) 8-19
- [44] J. Post, "*On the constitutive Behaviour of Sandvik NanoflexTM*", ISBN 90-6464-974-X (2004)
- [45] MSC Software Corporation, California, United States
- [46] M. Fukuhara, I. Yamauchi, "*Temperature dependence of the elastic moduli, dilational and shear internal frictions and acoustic wave velocity for alumina, (Y)TZP and β -sialon ceramics*", Journal of Materials Science 28 (1993) 4681-4688
- [47] <http://www.continuummechanics.org/cm/beambending.html>
- [48] E. Orowan, "*Proc, Instn. Mech. Engrs,*" 151 (1944) 133 (discussion of paper by H. O'Neill)
Adapted from: J. Lubliner, "*Plasticity Theory*", Dover Publications, ISBN 978-0-486-46290-5 (1990)

Appendix A

To determine the effect of heat on the deformation of a sample under elastic stress, a bending test has been developed. The elastic stress is applied by bending a straight sample to a fixed radius. This is done by manufacturing a tool which clamps a sample between two fixed radii. In the design of the hinge and the radii, there is accounted for the thickness of the sample in such a way that the two radii are separated 0.5 mm (see figure 64 for the technical drawing of the tool). Loading of a sample is demonstrated in figure 63. After closure the clamps are locked with a wedge, inserted between a bolt and the top piece (figure 63(c)).

The samples are 14 cm long, 4 cm wide and are cut from a 0.5 mm thick steel sheet, with the long side in the rolling direction. For the measurements, two different bending tools have been used. Tool 1 induces a bending with a radius of 215 mm; tool 2 a radius of 160 mm.

The strain in the material during elastic bending is:

$$\epsilon = \frac{L - L_0}{L_0} = \frac{\theta(\rho - \gamma)}{\theta\rho} = -\frac{\gamma}{\rho}, \quad (33)$$

where L_0 is the length of the neutral axis, ρ the radius of curvature and θ the angle as shown in figure 62. This model does not distinguish between tension and compression:

$$\epsilon_{compressive} = -\epsilon_{tensile}, \quad (34)$$

with the assumption that the neutral axis has a minor change from position during the process. For the samples used in this test, $\gamma = 0.25$ mm.

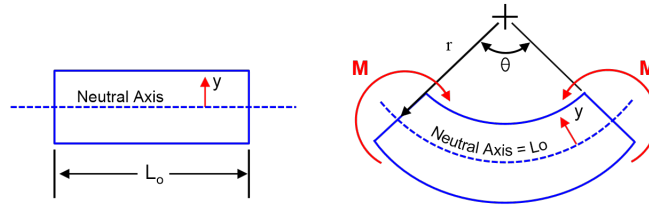


Figure 62: *Definitions of elastic bending [47].*

Experimental procedure

The holder (bending tool) without the sample is placed in an induction heating furnace and its temperature constantly monitored with a thermocouple, which is inserted in a hole on the side of the holder. The holder is pre-heated slightly above the desired temperature, since part of the heat is radiated very fast during loading. By trial and error and depending on the working speed, an overshoot of 30 °C is found to compensate for the heat loss during loading. After unloading, the samples are cooled in water and their radius measured.

Combining Hooke's law and equation 33, the stress σ in the top part of the sample becomes:

$$\sigma = -\frac{\gamma}{\rho}E, \quad (35)$$

Bending experiments are performed at three temperatures, their calculated induced stresses are shown in table 12. Equation 16 is used for the values of the E-modulus at these temperatures.

Temperature (°C)	Stress (Mpa) of Radius 1 (160 mm)	Stress (Mpa) of Radius 2 (215 mm)
500	219	163
600	199	148
700	178	132

Table 12: Calculated induced stress on the top of a sample of 0.5 mm thickness.



(a)



(b)



(c)

Figure 63: *Tool (a) for bending a straight sample (b) to a fixed radius (c).*

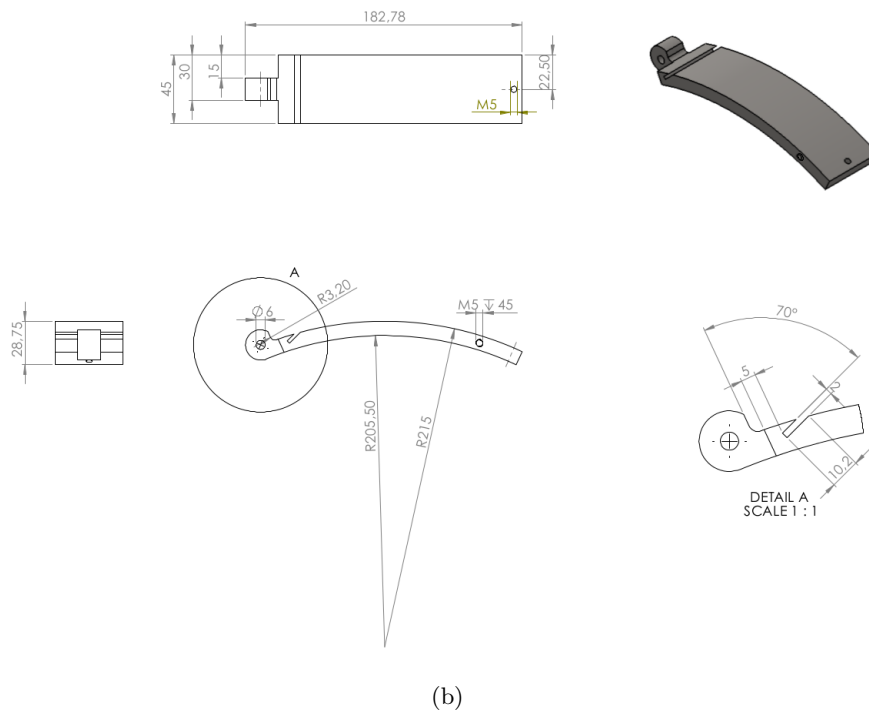
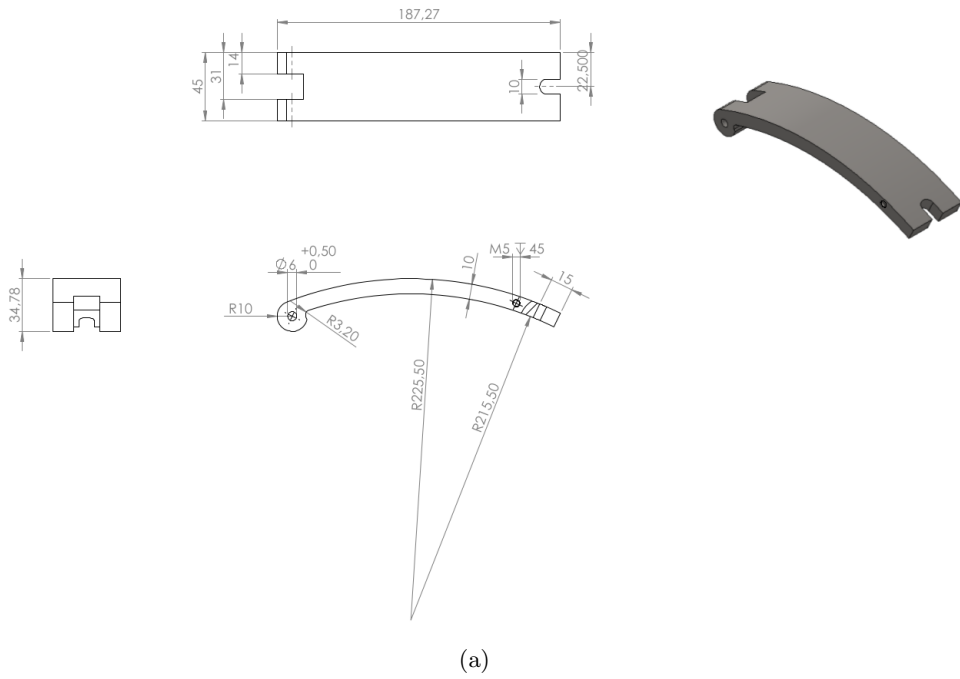


Figure 64: *Technical drawing of tool for bending test.*

Results

The results of bending tests are shown in figure 65. The induced bending loads differ from table 12, because of the spread in thickness of the samples. The results in figure 65(a) are comparable to the results of the stress relaxation test performed on the tensile machine. The difference can be caused through the bending in the samples by the coil, whereby the induced stress by the bending tool is smaller. Also the E-modulus which has been used for the calculation of the stress could be too low, resulting in an apparently lower stress. The stresses in figure 65(c) appear to increase in time. Partly, this can be caused by further bending of the sample at removal from the bending tool. Through erroneous values taken for the curvature of the bending tool, the stress at 600 °C and 700 °C is too high, causing plastic deformation. Therefore, these results are not reliable.

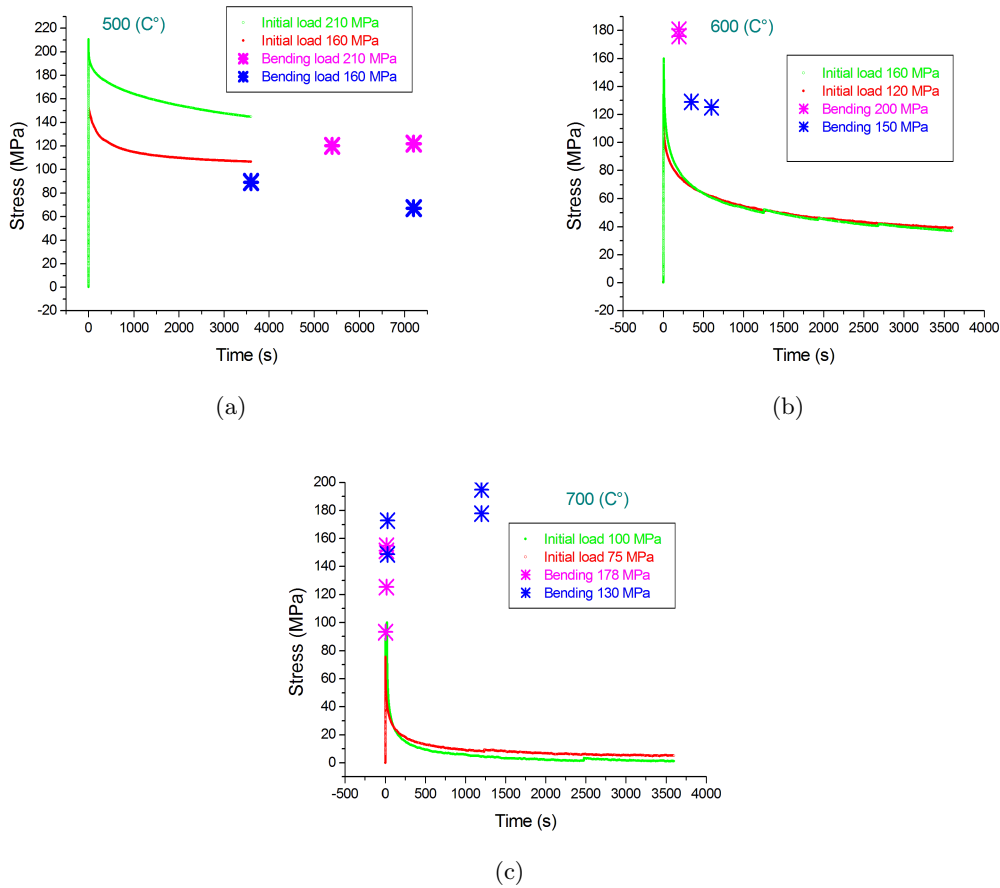


Figure 65: *Stress relaxation of bending test compared to stress relaxation of a tensile test.*

In conclusion: the bending tool can be used to obtain stress relaxation results. However, for further experiments it is necessary to obtain precise values of the E-modulus for these temperatures, whereupon the bending tool can be designed such that the applied load on the sample is below the yield point and the calculation of the stress with equation 35 is more accurate.

Appendix B

Input file for the FE calculation of a creep test at 700 °C for 30 seconds.

```
$ SOLVER input file for project: One_element, step: Step1
$ Generated by PreCrystal v1.46 (July 27, 2012) (project version 1.13)
$-----
$-----
$ Type analyse
$-----
$*DEBUG
$2000000 2000000 2 1
*$AXISYMMETRIC
$-----
$ Geometrie en materiaal beschrijving
$-----
*$READ_PRODUCT
$-----
$ Gereedschap beschrijving
$-----
*$REMESH_OFF
*$POST_BINARY
*$DIE_OUTPUT
*$AMBIENT_TEMP
  2.930E+02
$
$ Die number: 1, name: links
$
*$DIE_DEFINITION
  0.0000E-00 -1.0000E+00
  1.2858E-16  1.5000E+00  1.0000E-01
-1.1000E+00  1.5000E+00
$
$ Die number: 2, name: rechts
$
*$DIE_DEFINITION
  1.0000E+00 -1.0000E+00
  1.0000E+00  1.5000E+00  1.0000E-01
  2.1000E+00  1.5000E+00
*$DIE_THERM
1 0.0 293.0
2 0.0 293.0
*$DIE_NO_SEPARATION
1
2
$-----
$ Proces beschrijving
```

```

$-----
$ Definitie van processtap
$ bod = Body(Die) nummer
$ dof = richting; 1=x, 2=y
$ vel = snelheid
$ frc = kracht
$ bod, dof, vel or frc
$-----
$ Tijdsinterval van uitvoer
$-----
$
$ Processtap nummer: 1
$
*INCTIME
  0.300E-01
*POST
  0.300E-01
*DIE_FORCE
  1 1 -1.600E+02
$1 2 0.000E-00
*TIME
  1.000E-00
$-----
$
$ Processtap nummer: 2
$
*INCTIME
  0.300E-01
*POST
  0.300E+01
*UNIFORM_TEMP
  973
*TIME
  1.000E-00
$-----
$
$ Processtap nummer: 3
$
*INCTIME
  0.300E+00
*POST
  0.300E+00
*UNIFORM_TEMP
  973
*TIME
  3.000E+01

```

Appendix C

Code of the calculation of lookup tables 3 (*lup₃*), and 4 (*lup₄*) with the creep model.

```
function [lup_3,lup_4,T,sigma,controle]=creepfunction(data)

T=data.defin_var.temperature;
sigma=data.defin_var.von_mises;

%parameters are sigma and temperature T
%Temperature in Kelvin
%Sigma in MPa

for i=1:length(sigma)
    for j=1:length(T)

        E_m(j) = 2.0e+5 * (1.019 - 0.000651*(T(j)-273));

        if T(j) < 573 %no creep below 573 K
            A(j) = 0 ;
            Q_a(j) = 0;
            n(j) = 0;
        elseif T(j) > 773 & T(j) < 873
            A(j) = 10.^(-123.14 + (0.16342 * T(j)));
            n(j) = -23.409 + (0.033 * T(j));
            Q_a(j) = -589.41 + (0.83667 * T(j));
        else
            A(j) = 10.^(12.43 + (0.00812 * T(j)));
            n(j) = 6.273 - (0.001 * T(j));
            Q_a(j) = 141;
        end

        S_t = (sigma(i)/(E_m(j))).^(n(j)); %Stress term
        S_t = S_t / (sigma(i) + 1.000E-20); %Debugging: devide by the Von Mises.
        %Small number added to avoid '1/0'.

        R = 8.3114621; %gasconstant J/mol K
        e_term(j) = exp((-Q_a(j)*1000)/(R*(T(j))));

        dEdt(i,j)= (S_t.* A(j).* e_term(j));
        dEdT_estress(i,j)= dEdt(i,j).*sigma(i);

    end
end

lup_3=dEdt;
lup_4=dEdT_estress;
```

”The tensile test [is] very easily and quickly performed but it is not possible to do much with its results, because one does not know what they really mean. They are the outcome of a number of very complicated processes... The extension of a piece of metal [is] in a sense more complicated than the working of a pocket watch and to hope to derive information about its mechanism from two or three data derived from measurement during the tensile test [is] perhaps as optimistic as would be an attempt to learn about the working of a pocket watch by determining its compressive strength.”

E. Orowan [48]